Dirac Fermions in Solids: From High-T_c Cuprates and Graphene to Topological Insulators and Weyl Semimetals

Oskar Vafek[1] and Ashvin Vishwanath[2]

[1]National High Magnetic Field Laboratory and Department of Physics, Florida State University, Tallahassee, Florida 32306; email: vafek@magnet.fsu.edu

[2]Department of Physics, University of California, Berkeley, California 94720

Annu. Rev. Condens. Matter Phys. 2014. 5:83–112

First published online as a Review in Advance on January 2, 2014

The *Annual Review of Condensed Matter Physics* is online at conmatphys.annualreviews.org

This article's doi:
10.1146/annurev-conmatphys-031113-133841

Keywords

Dirac fermions, graphene, *d*-wave superconductors, topological insulators, Weyl semimetals

Abstract

Understanding Dirac-like fermions has become an imperative in modern condensed matter sciences: All across the research frontier, from graphene to high T_c superconductors to the topological insulators and beyond, various electronic systems exhibit properties that can be well described by the Dirac equation. Such physics is no longer the exclusive domain of quantum field theories and other esoteric mathematical musings; instead, physics of real condensed matter systems is governed by such equations, and important materials science and practical implications hinge on our understanding of Dirac particles in two and three dimensions. Although the physics that gives rise to the massless Dirac fermions in each of the above-mentioned materials is different, the low-energy properties are governed by the same Dirac kinematics. The aim of this article is to review a selected cross-section of this vast field by highlighting the generalities and contrasting the specifics of several physical systems.

1. DIRAC, WEYL, AND MAJORANA

> I think it is a peculiarity of myself that I like to play about with equations, just looking for beautiful mathematical relations which maybe don't have any physical meaning at all. Sometimes they do.
> - Paul A.M. Dirac (1902–1984)

Published in 1928 by Paul Dirac (1), the eponymous equation is among the finest achievements of human intellect. The equation, now taught in virtually every physics department around the world, has brought together Einstein's special theory of relativity and quantum mechanics. It led to the prediction of antimatter, namely the positron as the electron's antipartner. It casted the spin-1/2 nature of the electron in a new light and is now a key building block of the Standard Model of particle physics. For a free particle, it can be written as

$$i\hbar\frac{\partial}{\partial t}\psi = \left(c\boldsymbol{\alpha}\cdot\mathbf{p} + \beta mc^2\right)\psi, \qquad 1.$$

where the momentum operator $\mathbf{p} = -i\hbar\nabla = (p_x, p_y, p_z)$, m is the mass of the particle, c is the speed of light in vacuum, and ψ is a four-component object, a spinor. There are many equivalent ways to write the Dirac 4×4 matrices; utilizing the outer product (2) of the Pauli matrices,[1] one such way is $\boldsymbol{\alpha} = (\tau_3\otimes\sigma_1, \tau_3\otimes\sigma_2, \tau_3\otimes\sigma_3)$ and $\beta = -\tau_1\otimes 1$. The equation was originally intended for the electron, which is, of course, a massive, spin-1/2, charged particle, i.e., a Dirac fermion.

There is a certain degree of simplification occurring in this equation in the special case of massless particles. All three $\boldsymbol{\alpha}$ matrices are block diagonal, whereas the term proportional to the mass is block off-diagonal. Therefore, if we consider massless particles, the right-hand side of the Dirac equation no longer couples the upper two components of ψ (let's call them χ_+) and the lower two components (χ_-). Thus, with $m = 0$, it can be written in a simpler form:

$$i\hbar\frac{\partial}{\partial t}\chi_\pm = \pm c\boldsymbol{\sigma}\cdot\mathbf{p}\chi_\pm. \qquad 2.$$

This is the Weyl equation (3) and χ's are referred to as Weyl fermions.

Both of these equations involve real and complex numbers. Majorana noticed (4) that it is possible to write the Dirac equation—including the mass term—entirely in terms of real numbers (2). This can be accomplished by choosing the $\boldsymbol{\alpha}$ matrices to be purely real and the β matrix to be purely imaginary because then both the right-hand side and the left-hand side of the Dirac equation are purely imaginary. For example, $\boldsymbol{\alpha} = (-\tau_1\otimes\sigma_1, \tau_3\otimes 1, -\tau_1\otimes\sigma_3)$, and $\beta = \tau_1\otimes\sigma_2$ does the job. Once the equation is purely real, its solutions can also be chosen to be purely real. In quantum field theory, a real field describes a particle that is its own antiparticle.

This review is about how such equations provide an accurate description of some two- (2D) and three-dimensional (3D) nonrelativistic systems, where Dirac or Weyl fermions emerge as low-energy excitations. This review also describes how these excitations behave when subjected to external fields, and how to relate the perturbing potentials (e.g., scalar, vector, mass, etc.) that appear in the effective Dirac equation either to externally applied fields produced in a laboratory or to defects and impurity potentials. A few consequences of many-body interactions are also reviewed. We do not discuss any of the fascinating aspects of Majorana fermions in condensed matter; this topic has already been covered in Reference 5 and references therein. The main topics

[1] As usual, $\tau_1 = \sigma_1 = \begin{pmatrix} 0 & 1 \\ 1 & 0 \end{pmatrix}$, $\tau_2 = \sigma_2 = \begin{pmatrix} 0 & -i \\ i & 0 \end{pmatrix}$, and $\tau_3 = \sigma_3 = \begin{pmatrix} 1 & 0 \\ 0 & -1 \end{pmatrix}$.

of this paper form a vast area of physics, and we ask the reader to keep in mind that it is impossible to do it justice within the allotted space.

2. WHEN TO EXPECT DIRAC POINTS IN CONDENSED MATTER AND WHY

In a nonrelativistic condensed matter setting, the time evolution of any many-body state $|\Psi\rangle$ is governed by the Schrödinger equation:

$$i\hbar\frac{\partial}{\partial t}|\Psi\rangle = \mathcal{H}|\Psi\rangle, \qquad 3.$$

where $\mathcal{H}$ is the Hamiltonian operator. This Hamiltonian contains the kinetic energy of the electrons and ions, as well as any interaction energy among them. Our aim is to illustrate how and when we may expect the relativistic-like Dirac dispersion to arise from $\mathcal{H}$ in a cold nonrelativistic solid state. We do so first by pure symmetry considerations and then in a brief survey of several physical systems that realize Dirac-like physics. We assume that the heavy ions have crystallized and ignore their motion to the first approximation. As such, the role of heavy ions is solely to provide a static periodic potential that scatters the electron Schrödinger waves and, if the spin-orbit coupling is also taken into account, the electron spins. Given that, $\mathcal{H} \to \mathcal{H}_0 + \mathcal{H}_{int}$, where $\mathcal{H}_0$ includes all the one-body effects and $\mathcal{H}_{int}$ includes all the many-body electron-electron interaction effects.

According to the Bloch theorem, the energy spectrum $E_n(\mathbf{k})$ and the eigenstates $|\phi_{n,\mathbf{k}}\rangle$ of $\mathcal{H}_0$ can be described by a discrete band index, n, as well as by a continuous D-dimensional vector, $\mathbf{k}$, the crystalline momentum, which is defined within the first Brillouin zone. Consider now two distinct but adjacent energy bands, $E_{n+}(\mathbf{k})$ and $E_{n-}(\mathbf{k})$, and assume that for some range of $\mathbf{k}$ the two bands approach each other, i.e., the energy difference $|E_{n+}(\mathbf{k}) - E_{n-}(\mathbf{k})|$ is much smaller than the separation from any one of the rest of the energy bands. One way to derive the effective Hamiltonian for the two bands is to start with a pair of (orthonormal) variational Bloch states, $|u_\mathbf{k}\rangle$ and $|v_\mathbf{k}\rangle$, consistent with, and adapted to, the symmetries of $\mathcal{H}_0$. Given that, the effective Hamiltonian takes the form

$$\mathcal{H}_{eff} = \sum_\mathbf{k} \psi^\dagger_\mathbf{k} H(\mathbf{k}) \psi_\mathbf{k}, \qquad 4.$$

where the first component of the creation operator $\psi^\dagger_\mathbf{k}$ adds a particle (to the N-body state) in the single-particle state $|u_\mathbf{k}\rangle$ and antisymmetrizes the resulting $N+1$-body state. Similarly, the second component creates a particle in the state $|v_\mathbf{k}\rangle$ and

$$H(\mathbf{k}) = \begin{pmatrix} \langle u_\mathbf{k}|\mathcal{H}_0|u_\mathbf{k}\rangle & \langle u_\mathbf{k}|\mathcal{H}_0|v_\mathbf{k}\rangle \\ \langle v_\mathbf{k}|\mathcal{H}_0|u_\mathbf{k}\rangle & \langle v_\mathbf{k}|\mathcal{H}_0|v_\mathbf{k}\rangle \end{pmatrix} \equiv f(\mathbf{k})1_2 + \sum_{j=1}^{3} g_j(\mathbf{k})\sigma_j, \qquad 5.$$

where 1_2 is the unit matrix and σ_j are the Pauli matrices. The corresponding one-particle spectrum is

$$E_\pm = f(\mathbf{k}) \pm \sqrt{\sum_{j=1}^{3} g_j^2(\mathbf{k})}. \qquad 6.$$

For a general $\mathbf{k}$ point and in the absence of any other symmetries, $g_j(\mathbf{k}) \neq 0$ for each j. It is clear from the expression for $E_\pm(\mathbf{k})$ that the two bands touch only if $g_j(\mathbf{k}_0) = 0$ for each j at some $\mathbf{k}_0$.

In 3D, we can vary each of the three components of $\mathbf{k}$ and try to find simultaneous zeros of each of the three components of $g_j(\mathbf{k})$. To see that this may be possible without fine-tuning, note that in general each one of the three equations $g_j(\mathbf{k}) = 0$ describes a 2D surface in $\mathbf{k}$ space. The first two surfaces may generally meet along lines, and such lines may then intersect the third surface at points without additional fine-tuning. If such points exist, they generally come in pairs and the dispersion near each may be linearized. The effective Hamiltonian near one such point $\mathbf{k}_0$ takes the form

$$H(\mathbf{k}) = E_{\mathbf{k}_0} + \hbar \mathbf{v}_0 \cdot (\mathbf{k} - \mathbf{k}_0) 1_2 + \sum_{j=1}^{3} \hbar \mathbf{v}_j \cdot (\mathbf{k} - \mathbf{k}_0) \sigma_j. \quad 7.$$

If $\mathbf{v}_0 = 0$ and the three velocity vectors $\mathbf{v}_j$ are mutually orthogonal, $H(\mathbf{k})$ has the form of an anisotropic Weyl Hamiltonian. Of course, far away from $\mathbf{k}_0$ both bands may disperse upward or downward, in which case even if the Fermi level could be set to $E(\mathbf{k}_0)$, there would be additional Fermi surface(s).

In 2D, only two components of $\mathbf{k}$ can be freely varied, and therefore it is impossible to find simultaneous zeros of three functions $g_j(\mathbf{k})$ without additional fine-tuning. Simply stated, in general, three curves do not intersect at the same point. Therefore, in the absence of additional symmetries that may constrain the number of independent $g_j(\mathbf{k})$'s, the two levels avoid each other.

2.1. Dirac Points and Kramers Pairs

We have intentionally refrained from any discussion of the electron spin degeneracy, or time-reversal symmetry, which were not assumed to be present in the above discussion. For a number of physical systems considered below, the product of the time reversal and the space inversion leaves the crystalline Hamiltonian invariant. This symmetry implies that, at each $\mathbf{k}$, every electronic level is doubly degenerate because if $\phi_{\mathbf{k}}(\mathbf{r})$ is an eigenstate, then so is its orthogonal Kramers-like partner, $i\sigma_2\phi^*_{\mathbf{k}}(-\mathbf{r})$, where σ_2 acts on the spin part of the wave function. Therefore, the appropriate variational quadruplet of mutually orthogonal states that describes two nearby bands can be constructed from $u_{1\mathbf{k}}(\mathbf{r})|\uparrow\rangle + u_{2\mathbf{k}}(\mathbf{r})|\downarrow\rangle$; its partner, $-u^*_{1\mathbf{k}}(-\mathbf{r})|\downarrow\rangle + u^*_{2\mathbf{k}}(-\mathbf{r})|\uparrow\rangle$; and $v_{1\mathbf{k}}(\mathbf{r})|\uparrow\rangle + v_{2\mathbf{k}}(\mathbf{r})|\downarrow\rangle$, with its partner $-v^*_{1\mathbf{k}}(-\mathbf{r})|\downarrow\rangle + v^*_{2\mathbf{k}}(-\mathbf{r})|\uparrow\rangle$. In this four-dimensional subspace

$$H(\mathbf{k}) = f(\mathbf{k}) 1_4 + \sum_{j=1}^{5} g_j(\mathbf{k}) \Gamma_j, \quad 8.$$

where $\Gamma_1 = \tau_3 \otimes 1$, $\Gamma_2 = \tau_1 \otimes 1$, $\Gamma_3 = \tau_2 \otimes \sigma_3$, $\Gamma_4 = \tau_2 \otimes \sigma_1$, and $\Gamma_5 = \tau_2 \otimes \sigma_2$; the first Pauli matrix acts within the u,v space and the second within the Kramers doublets. Although the corresponding one-particle spectrum, $E_{\pm} = f(\mathbf{k}) \pm \sqrt{\sum_{j=1}^{5} g_j^2(\mathbf{k})}$, exhibits a twofold degeneracy at any $\mathbf{k}$, an intersection of two Kramers pairs requires finding simultaneous zeros of five $g_j(\mathbf{k})$'s. Clearly, the bands avoid each other because, even in 3D, this condition cannot be satisfied without additional symmetry. For example, if the spin-orbit interaction can be neglected and time-reversal symmetry is preserved—on the basis of our earlier assumptions, this also implies that space inversion is preserved—then the spin $SU(2)$ symmetry forces $g_3 = g_4 = g_5 = 0$. With such additional symmetry in 3D, the accidental degeneracy may happen along 1D $\mathbf{k}$-space curves and in 2D at nodal points.

2.2. Fermion Doubling: The Nielsen-Nynomiya Theorem and Ways Around It

The Nielsen-Nynomiya theorem states that it is impossible to construct a noninteracting lattice-hopping model with a net imbalance in the number of (massless) Dirac fermions with positive

and negative chirality, provided that certain weak restrictions apply. For example, the translationally invariant hopping amplitudes are assumed to decay sufficiently fast so that in momentum space the Hamiltonian is continuous. The full proof (6) makes use of homotopy theory and is beyond the scope of this review; pedagogical discussion of this "no-go" theorem can be found in Reference 7. Here we illustrate the basic idea behind it through a simple example in two space dimensions.

Consider a model with two bands that may touch, such as the one given in Equation 5, with $g_3(\mathbf{k}) = 0$. Then, $g_1(\mathbf{k})$ and $g_2(\mathbf{k})$ are smooth periodic functions of k_x and k_y. If the first function vanishes along some curve in the Brillouin zone, e.g., the red line in **Figure 1**, and the second vanishes along another curve (the blue line in **Figure 1**), then the places where the two curves intersect correspond to massless Dirac fermions. Periodicity guarantees that any intersection must occur at an even number of points, corresponding to an even number of massless fermions; just touching the two curves does not produce a Dirac fermion because at least one component of the velocity vanishes. Importantly, there is an equal number of partners with opposite chirality.

One way to remove half of the massless fermions is to bring back $g_3(\mathbf{k})$ and force it to vanish at only half of the intersections of the red and the blue curves in **Figure 1**. This gaps out the unwanted Dirac points, leaving an odd number of gapless points. Haldane's model for a quantum Hall effect without Landau levels is a condensed matter example in which such an effect occurs along the phase boundaries separating quantum Hall phases and trivial insulating phases (8). HgTe quantum wells are another example (9). In these quantum wells, such single-valley massless Dirac fermions have been experimentally realized at the phase boundary that separates the quantum spin Hall phase (10) and a trivial insulating phase. In the lattice regularization of the relativistic

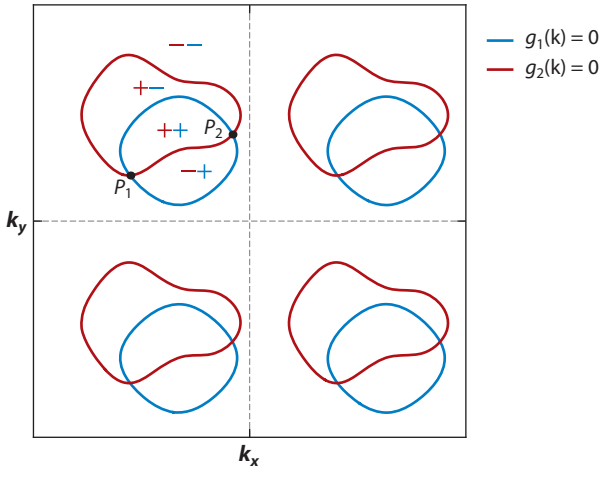

Figure 1

Illustration of the fermion doubling in the 2D lattice Hamiltonian. The blue and red lines correspond to the solutions of $g_1(\mathbf{k}) = 0$ and $g_2(\mathbf{k}) = 0$, respectively. Both $g_1(\mathbf{k})$ and $g_2(\mathbf{k})$ are smooth and must be periodic (for illustration, only four Brillouin zones are shown). Note that there is always an even number of intersections unless the two curves just touch. If we think of the two signs as points in the complex plane, we see that the gapless points have opposite chirality. Imagine displacing, e.g., the blue curve, down, holding the red curve fixed. The two points P_1 and P_2 then move toward each other and meet when the two curves touch. In this case, one of the Dirac velocities vanishes, and we do not have a Dirac fermion at all. Therefore, in any lattice formulation with finite range hopping, there is always an even number of (in general, anisotropic) massless Dirac fermions with opposite chirality.

high-energy theory, for which the space-time points are discrete and separated by at least a lattice constant, a, a similar term corresponds to the so-called Wilson mass term: a four-momentum dependent mass, $\sum_{j=0}^{3}\Delta\left(1-\cos(k_j a)\right)$, which vanishes at $\mathbf{k}=0$ and $\omega=0$. Adding the Wilson mass results in only one massless fermion, but it is not chiral. Moreover, in any condensed matter setting, making the $\mathbf{k}$-dependent mass term vanish at an isolated $\mathbf{k}$ point requires fine-tuning, and therefore such gapless points generally correspond to phase boundaries as opposed to phases (8, 10).

Another way of avoiding the fermion doubling on the lattice has been well known in high-energy theory (11, 12). Kaplan's idea has been to start with massive fermions and to make a mass domain wall along the nonphysical fourth spatial dimension, hereby labeled as w. By mass domain wall, we mean that for positive w the mass is m_0 and for negative w it is $-m_0$. For the $w=0$ lattice site, the mass vanishes. To this domain-wall mass term, add a 4+1D Wilson mass term. There is then a range of values of m_0 for which we have a single chiral 3+1D massless Dirac, i.e., Weyl, particle on the domain wall. For $m_0<2\Delta$, this can be understood as the two sides having a mass inversion at only one $\mathbf{k}$ point, namely at the origin. This was proposed as a method to simulate—on a lattice—chiral fermions in odd space-time dimensions: from 4+1D to 3+1D or from 2+1D to 1+1D.

Unlike the Wilson mass, its condensed matter reincarnation is frequency independent, although it is of course momentum dependent. Massless domain-wall fermions have been discussed by Volkov & Pankratov (13) at a 2D interface between (3D) SnTe and PbTe (see 14, 15). Such massless Dirac fermions are similar to those appearing at the surface of strong 3D topological insulators, although there is a difference: In the former case the mass sign change occurs at an even number of points in the Brillouin zone, whereas in the latter case the mass sign change occurs at an odd number of points (16, 17).

3. DIRAC PARTICLES SUBJECT TO EXTERNAL PERTURBATIONS

For relativistic Dirac fermions described by four-component spinors, external perturbations take the form of space-time dependent 4×4 matrices, which we denote by $V(\mathbf{r},t)$. In the Hamiltonian formalism,

$$H=\int d^3\mathbf{r}\psi^\dagger(\mathbf{r})\Big(c\boldsymbol{\alpha}\cdot\mathbf{p}+mc^2\beta+V(\mathbf{r},t)\Big)\psi(\mathbf{r}). \qquad 9.$$

There are 16 linearly independent 4×4 matrices that can be chosen for $V(\mathbf{r},t)$. In a relativistic context, their physical meaning is determined by their properties under Lorentz transformations.

1. If the matrix structure of $V(\mathbf{r},t)$ is the same as β, it clearly acts as a space-time varying mass; because it is a scalar under the Lorentz transformation, it is also sometimes referred to as a scalar potential (18).
2. Any $V(\mathbf{r},t)$ of the form $-e\boldsymbol{\alpha}\cdot\mathbf{A}(\mathbf{r},t)$ acts as the spatial component of the electromagnetic vector potential; it enters via minimal coupling.
3. If $V(\mathbf{r},t)=e\Phi(\mathbf{r},t)$, then it corresponds to the time component of the electromagnetic potential or, equivalently, the electrical potential.
4. Of the 11 remaining matrices, 6 are Lorentz tensor fields, 4 are pseudovectors, and 1 is pseudoscalar (18).

Before proceeding, it is important to stress that the appropriate V—which describes how Dirac fermions in a given condensed matter system react to, for example, an external physical magnetic field—depends on the system itself. For example, it is not the same in graphene and d-wave superconductors. This is elaborated on in later sections.

As mentioned earlier, for massless Dirac fermions the kinetic energy term $\boldsymbol{\alpha} \cdot \mathbf{p}$ can be chosen to be block diagonal. If the external perturbation $V(\mathbf{r}, t)$ does not couple the two Dirac points, then such perturbation is also block diagonal. In 2D, where $\mathbf{p}$ is a two-component vector, within each 2×2 block such perturbation can be identified as either a mass or a three-component electromagnetic potential, $\mathbf{A} = (\Phi, A_x, A_y)$. A constant mass term opens a gap in the spectrum; this gap may close at the boundaries or defects but persists in their absence. Simply put, for any energy $-m < E < m$, the equation $E^2 = c^2\mathbf{p}^2 + m^2$ forces $\mathbf{p}$ to be imaginary, and the corresponding states can at best be evanescent. A constant electric potential, Φ, shifts the energy eigenvalues; the constant space component A_x or A_y shifts the momentum. The situation is similar in 3D, except the 2×2 matrix, which in 2D could be identified with the mass-like term, does not open a gap in 3D. Rather, it also shifts the momentum, and therefore should be thought of as another space component of the vector potential.

Such simple intuitive arguments (19) show why Dirac particles can be confined by a spatially varying mass, but not by a spatially varying electric potential. This observation is behind the famous Klein paradox (20). Instead of confining the massless Dirac particles, such an electric potential causes a transfer of states toward the Dirac point, a situation loosely analogous to an impurity electric potential creating in-gap states in semiconductors.

A uniform electric field, $\mathbf{E} = -\nabla\Phi$, accelerates charged massless Dirac particles and leads to nonequilibrium phenomena; it produces charge electron-positron pairs out of the filled Dirac sea via the Schwinger mechanism (21). For massless Dirac particles in 2D, such a rate has been calculated to be $\sim (eE)^{3/2}$ (21, 22) and argued to lead to the electrical current increasing as $E^{3/2}$ above a finite field scale, below which it is E linear (23–25).

The effect of a static 1D plane-wave electrical potential, $\Phi(x, y) = \Phi_0 \cos(qx)$, on 2D massless Dirac fermions was considered in Reference 26. On the basis of our discussion in this review, we intuitively expect that such potential locally shifts the Fermi energy away from the Dirac point and introduces electron-positron "stripe puddles." The energy spectrum has a particle-hole symmetry: For every eigenstate $\psi_E(x, y)$ with an energy E, there is an eigenstate $\sigma_3\psi_E(x + \pi/q, y)$ with an energy $-E$. For this result, we assumed that the kinetic energy term is $c(p_x\sigma_1 + p_y\sigma_2)$. The full quantum mechanical solution of this problem, performed numerically using a large number of plane-wave states, shows that, although the energy spectrum remains gapless, the spectral weight is indeed shifted toward the Dirac point. This is shown in **Figure 2**, where we compare the integrated density of states, starting from $E = 0$, in the presence and absence of the periodic potential. Clearly there is an excess number of states at low energy. Interestingly, the lost states are recovered at energies comparable with the cutoff, which is much larger than Φ_0. Analogous buildup of the low-energy density of states underpins the interpretation of the measured low-temperature specific heat of type-II nodal d-wave superconductors in an external magnetic field, which is discussed below.

A uniform magnetic field directed perpendicular to the 2D plane, $B = \partial A_y/\partial x - \partial A_x/\partial y$, quantizes the electron orbits. The resulting spectrum consists of discrete Landau levels at energies $E_n = \mathrm{sgn(n)}\sqrt{|n|}\Omega_c$ where $n = 0, \pm 1, \pm 2, \ldots$, $\Omega_c = \sqrt{2}\hbar c/\ell_B$, and the magnetic length $\ell_B = \sqrt{\hbar c/eB}$; this result is easily obtained by elementary methods (for example, see 27). Therefore, unlike for a Schrödinger electron, the energy difference between the Landau levels of a massless 2D Dirac electron decreases with increasing energy. Each Landau level is N-fold degenerate, where $N = Area/(2\pi\ell_B^2)$; the degeneracy, being proportional to the sample area, is macroscopically large. As shown in **Figure 3**, the uniform magnetic field causes redistribution of spectral weight over the energy interval $(\sqrt{n+1} - \sqrt{n})\Omega_c$; the number of states that are moved to the Landau levels equals the total number of states that would be present between the Landau levels in the absence of the external B-field.

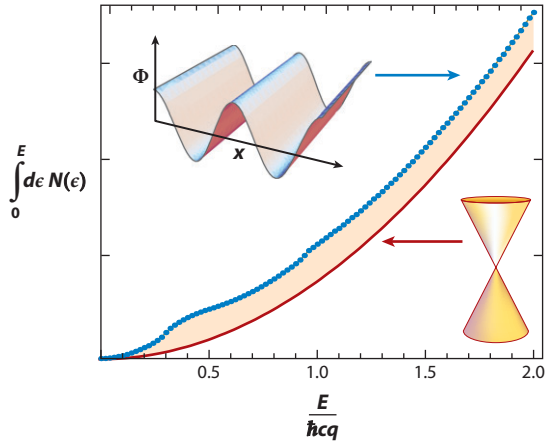

Figure 2

Integrated single-particle density of states for a massless Dirac fermion in 2D subject to a static 1D periodic electric potential $\Phi_0 \cos(qx)$ (*blue dots*), where $\Phi_0 = \hbar cq$; the solid red line corresponds to a free massless Dirac particle. The bottom right image shows the energy-momentum dispersion of a free Dirac particle, i.e., no external perturbation. The integrated density of states for this situation is shown in the red curve. The pale orange area between the curves is there to emphasize the difference between the blue curve (*dots*) and the red curve; this difference does not vanish as E increases. Note the buildup of the spectral weight, which is recovered only near the cutoff energy and is much larger than the scale shown.

The effects of a perpendicular magnetic field and an in-plane electric field have been studied in the context of proving the absence of the relativistic correction to the quantum Hall effect in ordinary 2D electron gas (28). The eigenfunctions and eigenvalues can be determined analytically, either directly (28), or, if $B > E$, by first Lorentz boosting the space-time coordinates and the Dirac spinors into a frame in which the electric field effectively disappears and only the Lorentz-contracted magnetic field enters (29) (we discussed this simpler problem above) and then inverse Lorentz boosting the wave functions and eigenenergies.

Effects of nonuniform Dirac mass are quite fascinating, particularly when the mass profile is topologically nontrivial and can lead to fractionalization of fermion's quantum numbers. We illustrate the effect for 1D Dirac particles, first published in 1976 by Jackiw & Rebbi (30). The kinetic energy and the mass term together give $H_{JR} = c\sigma_1 p + \sigma_3 m(x)$, where $m(x)$ is fixed to approach $\pm m_0$ as $x \to \pm\infty$, vanishing once somewhere in between. One such kink configuration is, for example, $m(x) = m_0 \tanh(x/\xi)$. The spectrum of H_{JR} is particle-hole symmetric because for any state $\psi_E(x)$ with energy E, there is a state $\sigma_2\psi_E(x)$ with energy $-E$. As we argued earlier, any midgap state with $-m_0 < E < m_0$ must be localized. Let us therefore seek states at $E = 0$; they must satisfy $i\hbar c\sigma_1\psi_0'(x) = m(x)\sigma_3\psi_0(x)$. If we substitute $\psi_0(x) = \sigma_1\chi_0(x)$, then we find $\hbar c\chi_0'(x) = m(x)\sigma_2\chi_0(x)$. The solution now follows immediately: $\chi_0(x) = N \exp\left[\frac{1}{\hbar c}\int_0^x dx' m(x')\sigma_2\right]\chi_0(0)$. Because any $\chi_0(0)$ can be decomposed into a linear combination of the $+1$ and -1 eigenvectors of σ_2, we see that because the term in the integral is positive, χ_0 must be purely the -1 eigenvector, $\begin{pmatrix} 1 \\ -i \end{pmatrix}$, otherwise the solution is not normalizable. There is therefore a single isolated energy level at $E = 0$. For a general single-kink mass profile, there may be other in-gap states, but they must come in pairs at nonzero energies $\pm E$.

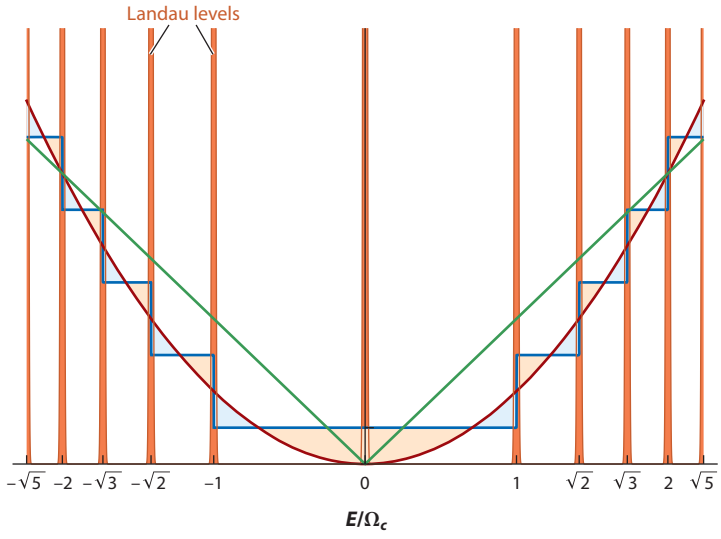

Figure 3

Single-particle density of states (*orange*) for a 2D charged massless Dirac fermion subject to a uniform magnetic field. The Landau levels have been broadened for easier visualization. The green line is the density of states for the free Dirac particle. Blue lines are the integrated density of states for the Dirac particle in an external magnetic field; the red line represents an unperturbed Dirac particle. The (step-like) integrated density of states shows that the spectral weight is redistributed over the energy window given by $\left(\sqrt{n+1}-\sqrt{n}\right)\Omega_c$, where $\Omega_c \equiv \sqrt{2}\hbar c/\ell_B$, and $\ell_B = \sqrt{\hbar c/eB}$ is the magnetic length. The pale blue and orange areas are there to emphasize the difference in the integrated density of states for the free Dirac particle and for the Dirac particle in the magnetic field.

The remarkable consequence of this isolation is that if the $E = 0$ midgap state is empty while all the negative energy states are occupied with charge e fermions, then the resulting state carries an excess localized charge of $-e/2$ relative to the ground state with uniform mass without a kink. Similarly, if it is occupied, the excess charge is $e/2$. This follows from the fact that a symmetric configuration of a widely separated kink and an antikink leads to a pair of essentially zero-energy states. In effect, one level has been drawn from the conduction band and one from the valence band, each of which are missing one state. If the zero-energy doublet is unoccupied, then the total charge of this state differs from the constant mass state by $-e$. Because the two localized states at the kink and the antikink are perfectly symmetric, we must find that the total amount of charge in the vicinity of each kink is the same, namely, $-e/2$ more than in the undistorted vacuum. If the vacuum is neutral, then each kink carries a half-integral charge. Given that in any physical setup with periodic boundary conditions every kink must have a corresponding antikink, the quantum number fractionalization happens only locally. Globally, the charge changes by integral units. Interestingly, if the particle-hole symmetry is weakly broken by adding to H_{JR} a small constant term proportional to σ_2, then the localized states carry an irrational charge (31). Such ideas have fascinating applications to the physics of conducting polymers (32, 33), and there is an extensive literature on the subject reviewed in Reference 34.

In higher dimensions, the topologically nontrivial configurations also lead to zero modes (30, 35). Just as in 1D, such results are insensitive to the details of the mass configuration, and only the overall topology matters (36). As an illustration of an effect a nontopological configuration of the mass can have on a 2D massless Dirac fermion, we consider a 1D plane wave, $m(x, y) = m_0\cos(qx)$. The

resulting Hamiltonian, $c(p_x\sigma_1 + p_y\sigma_2) + m(x,y)\sigma_3$, has a particle-hole symmetry, in that for every eigenfunction $\psi_E(x,y)$ with energy E, there is an eigenfunction $\sigma_3\psi_E(x+\pi/q,y)$ with energy $-E$. The momentum along the y-axis, k_y, is conserved as a result of the translational symmetry in the y-direction. The momentum in the x-direction, k_x, is conserved only up to an integer multiple of the reciprocal lattice vector. At $k_x = k_y = 0$, we can construct the $E = 0$ state explicitly, just as we did for the Jackiw-Rebbi problem, but now both choices for χ_0 lead to Bloch normalizable wave functions. There is therefore a doublet of states at $\mathbf{k} = 0$ and $E = 0$. Away from $\mathbf{k} = 0$, there is a new anisotropic Dirac cone, with renormalized velocities. Interestingly, at $\mathbf{k} = 0$, the spectrum consists only of doublets at any energy because for every $\psi_E(x,y)$ there is $\sigma_2\psi_E^*(x+\pi/q,y)$, which is also found at $\mathbf{k} = 0$, has the same energy, and is orthogonal to $\psi_E(x,y)$. The overall effect on the integrated density of states is shown in **Figure 4** for $m_0 = \hbar cq$. The minimum of the second band is found at $E \approx 1.1\hbar cq$ and is responsible for the change of slope. Overall, there is a suppression of the number of states at low energy—an opposite effect compared with the electric potential case. Similarly, the lost states are recovered only at energies comparable with the cutoff, which is much larger than m_0.

To conclude this section, we briefly mention the chiral anomaly associated with the massless Dirac equation (37, 38). The anomalies in quantum field theory are a rich subject (39) and play a very important role in elementary particle physics (40). In order to illustrate the effect, note that the massless Dirac Hamiltonian in 3D and in the presence of an arbitrary external electromagnetic field, $\int d^3\mathbf{r}\psi^\dagger(\mathbf{r})\left(c\boldsymbol{\alpha}\cdot\left(\mathbf{p} - \frac{e}{c}\mathbf{A}(\mathbf{r},t)\right) + e\Phi(\mathbf{r},t)\right)\psi(\mathbf{r})$, formally commutes with both the total particle number operator—or equivalently, the total charge operator—$\int d^3\mathbf{r}\psi^\dagger(\mathbf{r})\psi(\mathbf{r})$ and the total chiral charge operator $\int d^3\mathbf{r}\psi^\dagger(\mathbf{r})\tau_3 \otimes 1\psi(\mathbf{r})$. Here we use the representation for $\boldsymbol{\alpha}$ used

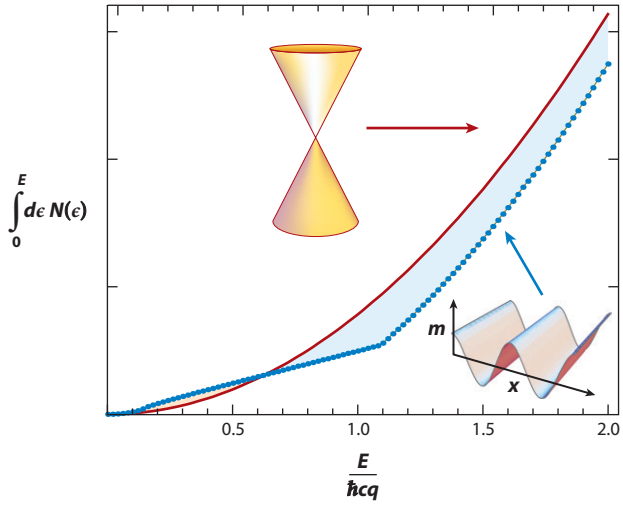

Figure 4

Massless Dirac fermion in 2D, which is subject to the 1D periodic mass $m(x,y) = m_0\cos(qx)$, with $m_0 = \hbar cq$. The top left image shows the energy-momentum dispersion of a free Dirac particle, i.e., no external perturbation. The integrated density of states for this situation is shown in the red curve. The pale blue and orange areas are there to emphasize the difference in the integrated density of states for the free Dirac particle and for (*bottom right image*) the Dirac particle perturbed by varying mass potential. Note the suppression of the spectral weight, which is recovered only near the cutoff energy and is much larger than the scale shown.

in Equation 1. The equation of motion for an operator $\mathcal{O}(t)$ in the Heisenberg picture is $d\mathcal{O}(t)/dt = \left[\mathcal{O}(t), H_H(t)\right]/i\hbar$, where $H_H(t)$ is the Dirac Hamiltonian in the Heisenberg representation. Because the commutator vanishes for both the total charge and the total chiral charge, they should both be constants of motion. However, closer inspection reveals that in explicit calculations (37, 38, 40), an ultraviolet regularization must be adopted in order to obtain finite results. What's more, if the regularization is chosen in such a way as to maintain the conservation of charge—a physically desirable consequence of a useful theory—then for some configurations of electromagnetic fields, the chiral charge is not conserved and changes in time. As an illustration, one such configuration consists of a uniform magnetic field along the z-direction and a parallel weak electric field (40). This can be described by $\Phi = 0$ and $\mathbf{A}(t) = \Big(-By, 0, A_z(t)\Big)$, where the electric field is given by $-\dfrac{1}{c}\dfrac{d}{dt}A_z(t)$; the time variation of $A_z(t)$ is therefore slow. For a system with size L^3 and periodic boundary conditions, the momentum is quantized in units of $2\pi/L$ and the separation between the adjacent energy levels is nonzero. If the rate of change of $A_z(t)$ is much smaller than the separation of the energy levels, then we can use the adiabatic theorem, solve for the eigenenergies using the instantaneous $A_z(t)$, and then monitor the energy spectrum in time. Such an energy spectrum is easily constructed once we notice that we are effectively dealing with $\pm\boldsymbol{\sigma}\cdot(c\mathbf{p} - e\mathbf{A})$. These are just two copies—with opposite signs of the Hamiltonian—of the Landau level problem of a massive Dirac particle in 2D, with the mass set by $c\hbar k_z - eA_z(t)$. The spectrum for each is given by $\pm\sqrt{\Big(c\hbar k_z - eA_z(t)\Big)^2 + n\Omega_c^2}$, where $n = 1, 2, 3, \ldots$, together with the two anomalous levels, one for each chirality, at $\pm\Big(c\hbar k_z - eA_z(t)\Big)$. If, at $t = 0$, we start with the many-body state, in which all negative energy single-particle states are occupied and all positive energy ones are empty, and then adiabatically increase A_z from 0 to hc/eL, then, while their energy is changing, none of the anomalous single-particle states change because their phase is locked by the periodic boundary condition. Once A_z reaches hc/eL, we can perform the gauge transformation that removes A_z from the Hamiltonian and that is consistent with the periodic boundary conditions, and find that we end up with the many-body state that appears to differ from the initial many-body state by the occupation of one additional negative chirality anomalous Landau level at energy hc/L and one fewer positive chirality Landau level at energy $-hc/L$. Note that the infinitely deep negative-energy Dirac sea plays a key role in this argument. Given that the degeneracy of each Landau level is $L^2/2\pi\ell_B^2$, we change the difference in the number of the positive and negative chirality states, $\delta N_+ - \delta N_-$, by $-2\Big(L^2/2\pi\ell_B^2\Big)(eL/hc)\delta A_z$. Relating δA_z to the electric field, we find

$$\Delta N_+ - \Delta N_- = \frac{1}{2\pi^2}\frac{e^2}{\hbar^2 c}\int dt \int d^3\mathbf{r}\,\mathbf{E}\cdot\mathbf{B}. \qquad 10.$$

This expression for the nonconservation of the total chiral charge is a direct consequence of the Adler-Bell-Jackiw anomaly.

4. MANY-BODY INTERACTIONS

In all condensed matter applications, the velocity of the massless Dirac particles, v_F, is much smaller than the speed of light in vacuum, c. This difference is important when many-body interactions are considered, and therefore, going forward, we intentionally distinguish between v_F and c.

In a 2D semimetal such as graphene, we can imagine integrating out all high-energy electronic modes outside of a finite energy interval around the Dirac point. The Fermi level is assumed to be close to the energy of the Dirac point. Because none of the gapless modes have been integrated out,

there can be no nonanalytic terms generated at long wavelengths, and, in particular, no screening of the $1/r$ electron-electron interaction in which a 2D Fourier transform is, of course, nonanalytic in momentum. Indeed, the long-distance tail of the bare electron-electron interactions falls off as $e^2/(4\pi\varepsilon_d r)$, where ε_d is the dielectric constant of the 3D medium in which the graphene sheet has been embedded. At long distances, ε_d is independent of the screening within the graphene sheet coming from the core carbon electrons. This can be shown by solving an elementary electrostatic problem of a point charge inserted in the middle of an infinite dielectric slab of finite thickness placed in a 3D medium with a dielectric constant ε_d (41–43). At distances much greater than the thickness of the slab, the Coulomb field within the slab is entirely determined by ε_d. A finite on-site Hubbard-like interaction is usually invoked to model the very short–distance repulsion.

What then are the consequences of such electron-electron interactions if the Dirac point coincides with the Fermi level? The importance of each of the terms can be determined by dimensional analysis: In 2D, the Dirac field scales as an inverse length, and therefore the short-distance (contact) coupling g, multiplying four Dirac fields, has dimensions of length. In any perturbative series expansion, each power of g must be accompanied by a power of an inverse length to maintain the correct dimensions of a physical quantity that is being computed. Because it is critical, the only length scales in the problem are associated with finite temperature, i.e., the thermal length $\hbar v_F/k_B T$, or the wavelength (frequency) of the external perturbation. As such length scales become very long, each term in the perturbative series in g becomes small, and we expect the series to converge. In the parlance of critical phenomena, the short-range interaction is perturbatively irrelevant at the noninteracting (Gaussian) fixed point (for example, see 44). Therefore, although there can be finite modifications of the Fermi velocity or of the overlap of the true (dressed) quasiparticle with the free electron wave function, the asymptotic infrared properties of the model must be identical to the noninteracting Dirac problem (45, 46).

Using a similar analysis for the $1/r$ tail of the nonretarded Coulomb interaction, one finds that $e^2/(\varepsilon_d \hbar v_F)$ is dimensionless. Despite the superficial similarity with the 3+1D quantum electrodynamics (QED) fine structure constant $e^2/\hbar c$, the physics here is different. First of all, the charge, being a coefficient of a nonanalytic term in the Hamiltonian, does not renormalize when high-energy modes are progressively integrated out (47, 48). Any renormalization group flow of the dimensionless coupling $e^2/(\varepsilon_d \hbar v_F)$ must therefore originate in the flow of v_F, which is no longer fixed by the Lorentz invariance because such symmetry is violated by the instantaneous Coulomb interaction. Detailed perturbative calculations reveal (49) that v_F grows to infinity logarithmically at long distances, thereby shrinking $e^2/(\varepsilon_d \hbar v_F)$. Physically, however, v_F cannot exceed the speed of light, c. Instead, once the retarded form of the electron-electron interaction is properly included via an exchange of a 3D photon, the flow of v_F saturates at c. The resulting theory is quite fascinating, in that the 2D massless Dirac fermions and the 3D photons propagate with the speed of light and, unlike in 3+1D QED, the coupling $e^2/\hbar c$ remains finite in the infrared (49). Unfortunately, because the flow of v_F is only logarithmic, and because there is initially a large disparity in the values of v_F and c, such a fixed point is practically unobservable. Instead, in practice, the physics is at best given by the crossover regime in which v_F increases but never to values comparable with c.

The $1/r$ Coulomb interaction–induced enhancement of the Fermi velocity is expected to lead to a suppression of the low-temperature specific heat below its noninteracting value (50), as well as other thermodynamic quantities (51). Interestingly, the suppression of the single-particle density of states does not lead to a suppression of the a.c. conductivity; in the noninteracting limit, the conductivity takes the (frequency-independent) value $\sigma_0 = Ne^2/16\hbar$, where N is the number of the two-component "flavors." Again, the reason is the enhancement of the velocity: Loosely speaking, although there are fewer excitations at low energy, those that are left have a higher velocity and therefore carry a larger electrical current. The expression for the low frequency a.c. conductivity (52)

has the form $\sigma(\omega) = \sigma_0\left(1 + Ce^2\Big/\left(\hbar v_F + \frac{e^2}{4}\log\frac{v_F\Lambda}{\omega}\right)\right)$, where Λ is a large wave-number cutoff. In the limit $\omega \to 0$, the correction to the noninteracting value is seen to vanish (51–53). The value of the (positive) constant C in this expression has been a subject of debate, as it seems to depend on the details of the UV regularization procedure (52–57). Recently, the calculation of C within a honeycomb tight-binding model (58), which provides a physical regularization of the short-distance physics, found $C = 11/6 - \pi/2 \approx 0.26$; this value was also obtained within a continuum Dirac formulation using dimensional regularization (55) by working in $2 - \varepsilon$ space dimensions and eventually setting $\varepsilon = 0$.

Increasing the strength of the electron-electron interactions while holding the kinetic energy fixed is expected to cause a quantum phase transition into an insulating state with a spontaneously generated mass for the Dirac fermions (59, 60). Given that, as we just argued, weak interactions are irrelevant at long distances, such transition must happen at strong coupling, making it hard to control within a purely fermionic theory. The full phase diagram also depends on the details of the interaction and is difficult to determine reliably using analytical methods. However, if one assumes that there is a direct continuous quantum phase transition between the semimetallic phase at a weak coupling as well as a known broken-symmetry strong coupling phase (e.g., an antiferromagnetic insulator), then the critical theory can be argued to take the form of massless Dirac fermions Yukawa-like coupled to the self-interacting order parameter bosonic field (61). The advantage of this formulation is that the upper critical (spatial) dimension is three, and therefore such theory can be studied in $3 - \varepsilon$ space dimensions within a controlled ε-expansion, eventually extrapolating to two space dimensions by setting $\varepsilon = 1$. The transition thus found is indeed continuous and governed by a fixed point at finite Yukawa and quartic bosonic couplings. For the leading order in ε, the critical exponents have been determined (61); for the semimetal to the antiferromagnetic insulator quantum phase transition, the correlation length exponent $\nu = 0.882$ and the bosonic anomalous dimension is $\eta_b = 0.8$. Given that the dynamical critical exponent has been found to be $z = 1$, these values imply that the order parameter vanishes at the transition as $|u - u_c|^\beta$ with the exponent $\beta = 0.794$; here, u_c is a critical interaction. The $1/r$ Coulomb interaction has been found to be irrelevant at this fixed point.

Given that at half-filling the theory does not suffer from the fermion sign problem, a very promising theoretical approach in this regard is numerical. The Hubbard model on the honeycomb lattice, with the nearest neighbor hopping energy t and the repulsive on-site interaction U, has been studied using quantum Monte Carlo methods (62–65). Recent simulations on clusters consisting of as many as 2,592 sites show strong indications of a direct continuous phase transition at $U/t \approx 3.869 \pm 0.013$ between the (Dirac) semimetal and the antiferromagnetic insulator (65), disfavoring earlier claims (64) on the existence of a spin liquid phase for intermediate values of couplings $3.4 \lesssim U/t \lesssim 4.3$ using smaller cluster sizes of up to 648 sites. The critical exponent $\beta = 0.8 \pm 0.04$ extracted in Reference 65 is in excellent agreement with the value obtained using the analytic Yukawa-like theory (61). In subsequent numerical simulations, the antiferromagnetic order parameter has been pinned by introducing a local symmetry breaking field (66). The resulting induced local-order parameter was found far from the pinning center and measured. This procedure resulted in an improved resolution, confirming a continuous quantum phase transition between the semimetallic and the insulating antiferromagnetic states. The single-particle gap was found to track the staggered magnetization, whereas the critical exponents obtained from finite size scaling agree with those obtained from the leading order in ε-expansion (61).

The $1/r$ Coulomb interaction can also be simulated efficiently without the fermion sign problem by means of a hybrid Monte Carlo algorithm (67) using either staggered fermions (67–69)

or, preferentially, a honeycomb tight-binding lattice (70–74). The critical strength of the interaction necessary to achieve a quantum phase transition into an insulating state seems to depend on the details of the short-distance part of the repulsion. Moreover, the system sizes studied numerically (74) may be too small to explore the unscreened long-distance tail of the $1/r$ interactions and to therefore unambiguously establish theoretically whether suspended monolayer graphene should be insulating. It is worth pointing out here that experiments on the suspended high-purity monolayer graphene samples show no sign of spontaneous symmetry breaking and would thus place it on the semimetallic side of the phase diagram.

5. APPLICATIONS TO VARIOUS PHYSICAL SYSTEMS

5.1. Graphene

It is interesting to consider the massless Dirac fermions in graphene (75) within the perspective outlined above. Pure symmetry arguments are a powerful tool in this regard; our goal is to carry out such arguments in full detail in this section in order to illustrate their utility. Assuming a perfectly flat, sp^2-hybridized carbon sheet, the relevant atomic orbitals forming both the conduction and the valence bands are the carbon $2p_z$ orbitals (27, 75). A good variational ansatz for $u_{1\mathbf{k}}(\mathbf{r})$ is $\sum_{\mathbf{R}} e^{i\mathbf{k}\cdot\mathbf{R}}\phi_{p_z}\left(\mathbf{r}-\mathbf{R}-\frac{1}{2}\boldsymbol{\delta}\right)$, where $\phi_{p_z}(\mathbf{r})$ is a Löwdin orbital[2] with the same symmetry as the atomic p_z orbital (76). The exact form of the Löwdin orbital is unimportant for us in this review; its symmetry is what matters. In an idealized situation, without externally imposed strains or any other lattice distortions, the set of vectors $\mathbf{R}$ could be chosen to span the triangular sublattice of the graphene honeycomb lattice: $m\mathbf{R}_1+n\mathbf{R}_2$, with $\mathbf{R}_1=\sqrt{3}\hat{x}$, $\mathbf{R}_2=\frac{1}{2}\mathbf{R}_1+\frac{3}{2}a\hat{y}$ and m and n being integers. The basis vector $\boldsymbol{\delta}=\frac{\sqrt{3}}{2}a\hat{x}+\frac{1}{2}a\hat{y}$. Note that this Bloch state is manifestly periodic in $\mathbf{k}$. Similarly, we can choose $v_{1\mathbf{k}}(\mathbf{r})$ as $\sum_{\mathbf{R}} e^{i\mathbf{k}\cdot\mathbf{R}}\phi_{p_z}\left(\mathbf{r}-\mathbf{R}+\frac{1}{2}\boldsymbol{\delta}\right)$. This physically motivated choice, along with $u_{2\mathbf{k}}(\mathbf{r})=v_{2\mathbf{k}}(\mathbf{r})=0$, defines the four basis states used to construct Equation 8.

A flat graphene sheet is invariant under the mirror reflection around the plane of the lattice, which further constrains $H(\mathbf{k})$. Such an operation reverses the in-plane components of the electron spin—an axial vector—and leaves the perpendicular component unchanged, thus acting on the spin state as a π-rotation around the axis perpendicular to the graphene sheet. Additionally, the p_z orbitals are odd under the mirror reflection. Therefore, the effective Hamiltonian in Equation 8 is constrained to satisfy $1\otimes\sigma_3\, H(\mathbf{k})\, 1\otimes\sigma_3 = H(\mathbf{k})$ for any in-plane $\mathbf{k}$. This forces $g_4=g_5=0$ in Equation 8. Because the remaining three g_i's are, in general, nonzero, we see that with only two components of $\mathbf{k}$ we cannot find simultaneous zeros of three independent functions. Therefore, in the absence of any other symmetry, we should expect level repulsion.

We can find the location of the Dirac points by taking into account additional symmetries. The space inversion symmetry, e.g., around the center of the honeycomb plaquette, requires $\tau_1\otimes 1\, H(-\mathbf{k})\, \tau_1\otimes 1 = H(\mathbf{k})$. This forces $g_1(\mathbf{k})$ and $g_3(\mathbf{k})$ to be odd under $\mathbf{k}\to -\mathbf{k}$ and $g_2(\mathbf{k})$ to be even. If the lattice also has a threefold symmetry axis perpendicular to the sheet and passing through the plaquette center, then g_2 and g_3 must vanish at the two inequivalent points

[2]The Löwdin orbitals, as used by Slater & Koster (76), are linear combinations of the atomic orbitals that are orthogonal to each other on different sites.

$\mathbf{k} = \pm\mathbf{K} = \pm\frac{4\pi}{3\sqrt{3}a}\hat{x}$, as well as, of course, all points equivalent to $\pm\mathbf{K}$ by periodicity in the momentum space. This follows from our formalism when we note that the effect of the $\frac{2\pi}{3}$ rotation, induced on our wave functions by the operator $e^{-i\frac{2\pi}{3\hbar}\hat{L}_z}e^{-i\frac{\pi}{3}\sigma_3}$, affects our four basis states as $e^{i\phi\tau_3\otimes\sigma_3}e^{-i\frac{\pi}{3}1\otimes\sigma_3}$, where $\phi = \mathbf{k}'\cdot\mathbf{R}_1$ and $\mathbf{k}'$ are the result of rotating $\mathbf{k}$ 120° counterclockwise. The identity $e^{i\phi\tau_3\otimes\sigma_3}H(\mathbf{k}')e^{-i\phi\tau_3\otimes\sigma_3} = H(\mathbf{k})$ evaluated at $\mathbf{k} = \pm\mathbf{K}$ immediately leads to $g_2(\pm\mathbf{K}) = g_3(\pm\mathbf{K}) = 0$. Interestingly, g_1 is finite at $\pm\mathbf{K}$ with vanishing derivatives, although if we also assumed spin $SU(2)$ symmetry, which allows us to flip the spins using $\tau_1\otimes\sigma_1$, then g_1 would vanish as well. In such a case, irrespective of the microscopic details of the full Hamiltonian, the two bands must touch at $\pm\mathbf{K}$.

The Dirac particles of graphene therefore live at $\pm\mathbf{K}$. Strictly speaking, they are not quite massless because of nonzero spin-orbit coupling, which makes $g_1(\mathbf{k})$ finite. Such a term has been introduced by Kane & Mele (77). However, this term is very small in planar graphene structures because the carbon atom is light and because graphene has a reflection symmetry around the vertical plane that passes through the nearest neighbor bond (78, 79). There is therefore only a negligibly small Dirac mass at $\mathbf{K}$ of order 10^{-3} meV.

Expanding $H(\pm\mathbf{K}+\delta\mathbf{k})$ to first order in $\delta\mathbf{k}$ we find

$$H_{eff} = \pm m_{QSH}\tau_3\otimes 1 \pm \hbar v_F\delta k_\parallel\tau_1\otimes 1 + \hbar v_F\delta k_\perp\tau_2\otimes\sigma_3, \qquad 11.$$

where the threefold rotational symmetry guarantees that the $\delta k_\parallel$ and $\delta k_\perp$ are two mutually orthogonal projections of $\delta\mathbf{k}$. In the coordinate system we have adopted, the mirror reflection symmetry around the $x-z$ plane forces $\delta k_\parallel = \frac{1}{2}\delta k_x + \frac{\sqrt{3}}{2}\delta k_y$ and $\delta k_\perp = -\frac{\sqrt{3}}{2}\delta k_x + \frac{1}{2}\delta k_y$. At energy scales much smaller than m_{QSH}, this Hamiltonian describes the quantum spin Hall state: a gapped phase with counter-propagating edge states (77). As a result of the smallness of m_{QSH} in graphene, for all practical purposes we can set it to zero. The particle-hole asymmetry, which arises from the $\delta\mathbf{k}^2$ dependence of g_1, is also small in that it guarantees that the Fermi level can in principle be tuned to the Dirac point without the appearance of additional Fermi surfaces. The value for the Fermi velocity, $v_F \approx 10^6 m/s$, can be obtained from approximate first-principle calculations or from experiments.

5.1.1. Coupling to external fields. Perhaps the greatest utility of the Dirac-like Equation 11 is its abilityto capture the kinematics of the low-energy excitations and their dynamics when subjected to external, or internal, fields. The former are of course the experimental tools of choice in studying the system.

In our theoretical description, we are tempted to minimally couple the external vector potential $\mathbf{A}(\mathbf{r})$, which is associated with the perpendicular magnetic field $\mathbf{B}(\mathbf{r}) = \nabla\times\mathbf{A}(\mathbf{r})$, and the scalar potential associated with either an applied electric field or the field induced by impurities. Although some care must be applied because we are working with a Bloch basis whose periodic part changes with $\mathbf{k}$, to the order in small $\delta\mathbf{k}$ that the Equation 11 has been written, we are allowed to perform such minimal substitutions (80, 81). Therefore, as long as the fields are sufficiently weakly varying in space or, for the uniform magnetic field, as long as the magnetic length $\sqrt{\hbar c/eB}$ is much longer than the lattice spacing, we have

$$H_{eff} = \pm v_F\left(p_\parallel - \frac{e}{c}A_\parallel(\mathbf{r})\right)\tau_1\otimes 1 + v_F\left(p_\perp - \frac{e}{c}A_\perp(\mathbf{r})\right)\tau_2\otimes\sigma_3 + U(\mathbf{r})1_4 + H_Z, \qquad 12.$$

where the Zeeman term is $H_Z = \frac{1}{2}g\mu_B(B_x\tau_1\otimes\sigma_1 + B_y\tau_1\otimes\sigma_2 + B_z 1\otimes\sigma_3)$. The above Hamiltonian governs the behavior of graphene in an external magnetic field. The resulting Landau level

structure has been directly observed in scanning tunneling spectroscopy (82–84). The Hamiltonian's utility in understanding the experiments on graphene heterojunctions has been reviewed in Reference 20. The Schwinger mechanism, discussed in Section 3, has been experimentally tested in Reference 85. H_{eff} can also accommodate a time dependence of external potentials, important for interpreting the optical (86) or infrared (87) spectroscopy measurements of graphene. The enhancement of the Fermi velocity, which, as discussed in Section 4, is a signature of electron-electron interactions, have been reported in Reference 88, with no signs of gap opening at the Dirac point. The effects of strain, as an effective potential in H_{eff}, are discussed in References 89, 90, and 91. By and large, realistic impurity potentials in graphene cannot be treated in linear response theory (81, 92). A review of transport effects can be found in Reference 93.

5.2. Surface States of a 3D Topological Insulator

An example of a 3D topological insulator (16, 17, 94, 95) is Bi_2Se_3 (96–98). Its excitation spectrum is gapped in the 3D bulk, but its 2D surfaces accommodate gapless excitations that carry electrical charge and conduct electricity, and the dispersion of the surface excitations obeys massless Dirac equations. Unfortunately, presently the actual material suffers from imperfections causing finite bulk conductivity, a complication that we largely overlook in this review.

The electronic configuration of *Bi* is $6s^2 6p^3$ and of *Se* is $4s^2 4p^4$. Because the *p*-shells of *Se* lie ~ 2.5 *eV* below *Bi* (99), a naive valence count would suggest that the two *Bi* atoms donate six of their valence *p*-electrons to fill the *p*-shell of *Se*. We would therefore incorrectly conclude that the system is a simple, or trivial, insulator with a fully filled *Se*-like *p*-band and empty *Bi*-like conduction band, perhaps with an appreciable band gap. Interestingly, the strong spin-orbit coupling causes a band inversion (96, 97) near the Γ-point (the origin of the Brillouin zone), where the *Bi*-like states lie below the *Se*-like states. Because the rhombohedral crystal structure of Bi_2Se_3 has a center of inversion, the exact Bloch eigenstates must be either even or odd under space inversion at the crystal momenta that map onto themselves under time reversal, up to an integer multiple of a reciprocal lattice vector, i.e., $\mathbf{k} = -\mathbf{k} + \mathbf{G}$. Clearly, Γ is such a point. As shown by Fu & Kane (17), a sufficient condition for a band insulator with a center of inversion to be a 3D topological insulator is if such band inversion happens at an odd number of time-reversal invariant points. More precisely, the system is a 3D topological insulator if the product of the parity eigenvalues of the occupied bands at the time-reversal invariant $\mathbf{k}$ points is odd, with the understanding that we count the parity eigenvalue of only one of the members of the Kramers pair. This is indeed what happens within a more realistic band structure calculation (96, 97) of Bi_2Se_3. At the Γ point—but not at the other time-reversal invariant $\mathbf{k}$ points—the *Bi* p_z-like states are spin-orbit coupled to the more energetic $p_x \pm ip_y$-like *Bi* states (a parity-even combination) and get pushed below the parity-odd combination of the *Se* p_z-like and $p_x \pm ip_y$-like states.

Equation 8 describes the dispersion near the Γ point inside the bulk of the 3D system. This can be seen explicitly if we choose $u_{1\mathbf{k}}(\mathbf{r})$ to be predominantly made of the parity-even combination of *Bi* p_z-like orbitals and $-u_{2\mathbf{k}}(\mathbf{r})$ of the *Bi* $p_x + ip_y$-like orbitals; i.e., the states that are mixed because of the spin-orbit interaction. Similarly, for the proximate band, we have $v_{1\mathbf{k}}(\mathbf{r})$ made predominantly of the parity-odd combination of the *Se* p_z-like orbitals, with $-v_{2\mathbf{k}}(\mathbf{r})$ made of *Se* $p_x + ip_y$-like orbitals (97). Up to the quadratic order in deviation from the Γ point, $g_1(\mathbf{k}) = M_0 + M_1 k_z^2 + M_2(k_x^2 + k_y^2)$, with $M_0 < 0$ and $M_{1,2} > 0$. No $\mathbf{k}$-odd terms are allowed here because the states are of definite parity. Note that because M_0 is negative, in the immediate vicinity of the Γ point the *Bi*-like states lie below the *Se*-like states. At higher $\mathbf{k}$, we revert to the expected band ordering. For the other terms in Equation 8, $g_2(\mathbf{k}) = 0$ to linear order in $\mathbf{k}$ because of additional threefold rotational symmetry; $g_2(\mathbf{k})$ is nonzero when we include terms

up to order k^3 because the **k**-cubic invariant exists. The remaining terms must be **k** odd, because they couple opposite parity states: to linear order in small **k**, $g_3(\mathbf{k}) = B_0 k_z$, $g_4(\mathbf{k}) = -A_0 k_x$, and $g_5(\mathbf{k}) = -A_0 k_y$, where $A_0 \gtrsim B_0 > 0$. The particle-hole symmetry breaking term $f(\mathbf{k})$ is also finite, but given that its presence leads to the qualitatively same conclusions, it is ignored (97).

Given that $g_1(\mathbf{k})$ is finite at Γ, which in this approximation is the only place where g_3, g_4, and g_5 vanish, the spectrum in the bulk is, of course, gapped. However, the surface is gapless. To see this explicitly (96, 97), consider a semi-infinite interface in the $x - y$ plane, set $k_x = k_y = 0$, and construct evanescent zero-energy states along the z-direction. There are always two such normalizable states, which can be used as a basis for the low-energy subspace. The effective surface Hamiltonian for small k_x and k_y can be obtained by sandwiching the bulk Hamiltonian between these two states. For macroscopically thick material, we can ignore the exponentially small overlap between the surface states, and we find $H_{surf} = \pm A_0(k_x\sigma_y - k_y\sigma_x)$, where the top sign is for the top surface $z = L$, and the bottom sign is for the bottom surface $z = -L$. A similar procedure along the right ($y = L$) and left ($y = -L$) surfaces leads to $H_{surf} = \pm(B_0 k_z\sigma_x + A_0 k_x\sigma_z)$. The effective Hamiltonians are simply related to each other by space inversion. In general,

$$H_{surf} = \hat{\mathbf{n}}' \cdot (\boldsymbol{\sigma} \times \mathbf{k}'), \qquad 13.$$

where $\hat{\mathbf{n}}'$ is obtained by rotating the normal to the surface $\hat{\mathbf{n}}$ by 180° around the z-axis, and $\mathbf{k}' = (-A_0 k_x, -A_0 k_y, B_0 k_z)$. We thus arrive at an equation for massless, anisotropic, Dirac particles. However, unlike in graphene, which has four "flavors," the surface of the 3D topological insulator can support only a single flavor.

5.2.1. Coupling to external fields, interactions, and disorder effects. The existence of a single Dirac flavor on the surface of the 3D topological insulator has important consequences for robustness of the surface states toward impurity disorder. The states at **k** and at $-\mathbf{k}$ have opposite spin, leading to the suppression of backscattering (100) and absence of localization for weak (electrical-potential) disorder (101–103). Theoretically, such a (noninteracting) system is always expected to display electrical conductivity that increases toward infinity as a logarithm of the system size. Recall that in graphene with a pair of Dirac cones at **K** and $-\mathbf{K}$, such backscattering is always present and therefore weak localization is expected to eventually set in (104, 105), although for smooth impurity potentials, the back scattering may be very small (106, 107).

Recent numerical study (108) of a topologically nontrivial 3D lattice model—with random on-site energy intentionally placed only on the surface of the 3D system—indicates that the effective continuum description with Dirac particles scattered by an electrical potential holds if the disorder strength is much weaker than the bulk gap ($\sim 0.3eV$ in Bi_2Se_3). The assertion is based on identification of Dirac-like features in a momentum-resolved spectral function, even when the translational symmetry of the lattice is broken by disorder. As the typical disorder strength increases beyond the 3D bulk gap value, the surface states appear diffusive. For even larger disorder strength, the outermost surface states are localized, but weakly disordered Dirac-like states reappear directly beneath it. Apparently, for large surface disorder, an interface between a strongly localized Anderson insulator and a topological insulator is formed (108). As such calculations were performed on finite-size systems, which are too small to detect an Anderson localization transition, it is presently impossible to conclude whether there is a true phase transition at zero temperature separating the weak, the moderate, and the strong disorder regimes. The combined effects of electrical potential disorder and electron-electron (Coulomb) repulsion have been studied in Reference 109 using the continuum Dirac approximation. The authors argue that 3D topological insulators are different from graphene and that the single Dirac flavor makes the

system metallic with finite conductivity at zero temperature. Transport properties of topological insulators have been reviewed in Reference 110.

Because the electron spin in 3D topological insulators is strongly coupled to its momentum, unlike in graphene, the Zeeman coupling to the external magnetic field does not lead to simple spin splitting. Rather, it opens up a gap, turning massless Dirac particles massive. To further illustrate the difference between the Dirac particles in a 3D topological insulator and graphene, consider the situation in which the external uniform magnetic field is applied along the z-axis, and the field is sufficiently strong to quantize the orbital motion of the surface electrons. The equation describing the states on the top and bottom surfaces is then

$$\left[\pm v_F\left(\left(p_x+\frac{e}{c}By\right)\sigma_y-p_y\sigma_x\right)+g_z\mu_B B\sigma_z\right]\psi(x,y,\pm L)=E\psi(x,y,\pm L), \qquad 14.$$

where $\hbar v_F = A_0$ and g_z is the effective Landé g-factor. Indeed, the Zeeman coupling acts as a Dirac mass and does not lead to the usual splitting of the spin degenerate energy levels. It is straightforward to find the eigenvalues of this operator provided we are sufficiently far from any edge. The resulting Landau level spectrum is

$$E_n=\pm\sqrt{2A_0^2\left(\frac{eB}{\hbar c}\right)n+\left(g_z\mu_B B\right)^2},\ n=1,2,3,\ldots \qquad 15.$$

$$E_0=g_z\mu_B B. \qquad 16.$$

The physics in a quantizing magnetic field differs from graphene near the edge in another important way: The top and bottom surfaces are coupled through the side surfaces. The applied magnetic field is parallel to the side surfaces, and therefore there is no Landau quantization along this surface; even the Zeeman term does not open up a gap on the side surfaces, it merely shifts the momentum by a constant. Therefore, as the guiding center of the Landau levels approaches the edge, they start mixing into the continuum of the states in the side surfaces. **Figure 5** shows the electronic spectrum of a 3D topological insulator semi-infinite slab of finite thickness versus the guiding center coordinate. Far away from any edges, the spectrum exhibits the usual Dirac Landau level quantization $E=\sqrt{n}\sqrt{2}\hbar v_F/\ell_B$, where $\ell_B=\sqrt{\hbar c/eB}$ and for Bi_2Se_3, $v_F = A_0$. Every such Landau level is doubly degenerate because the top and the bottom surfaces are assumed to be identical. Such degeneracy would be lifted if the inversion symmetry is broken by, for example, a constant chemical potential difference between the top and the bottom surfaces. As the guiding center coordinate approaches the right edge—or the outer edge for the Corbino geometry—the Landau level states merge with the plane-wave states from the vertical side surface. In the limit of very large thickness, such plane-wave states form a Dirac continuum.

This poses interesting questions: How robust is the quantum Hall effect and how can it be measured (111)? If the Fermi energy lies between the two Landau levels, the spectrum contains $M = 2n + 1$ chiral edge modes in addition to $2N$ nonchiral edge modes. Clearly, in any Hall bar geometry the leads necessarily couple to the continuum of the states in the side surfaces, which present additional (unwanted) channels of conduction. Assuming that the side modes equilibrate with each other and result in a finite conductivity, the chemical potential drops smoothly between μ_R and μ_L along each edge, and no quantization of Hall conductance is expected (111–113). Interestingly, quantization of σ_{xy} has been reported in a strained 70-nm-thick HgTe layer (114), with a well-developed plateau at $\nu = 2$ and plateau-like features at $\nu = 3$ and 4. At the same time, the longitudinal resistance R_{xx} measured at 50 mK shows suppression by few tens of

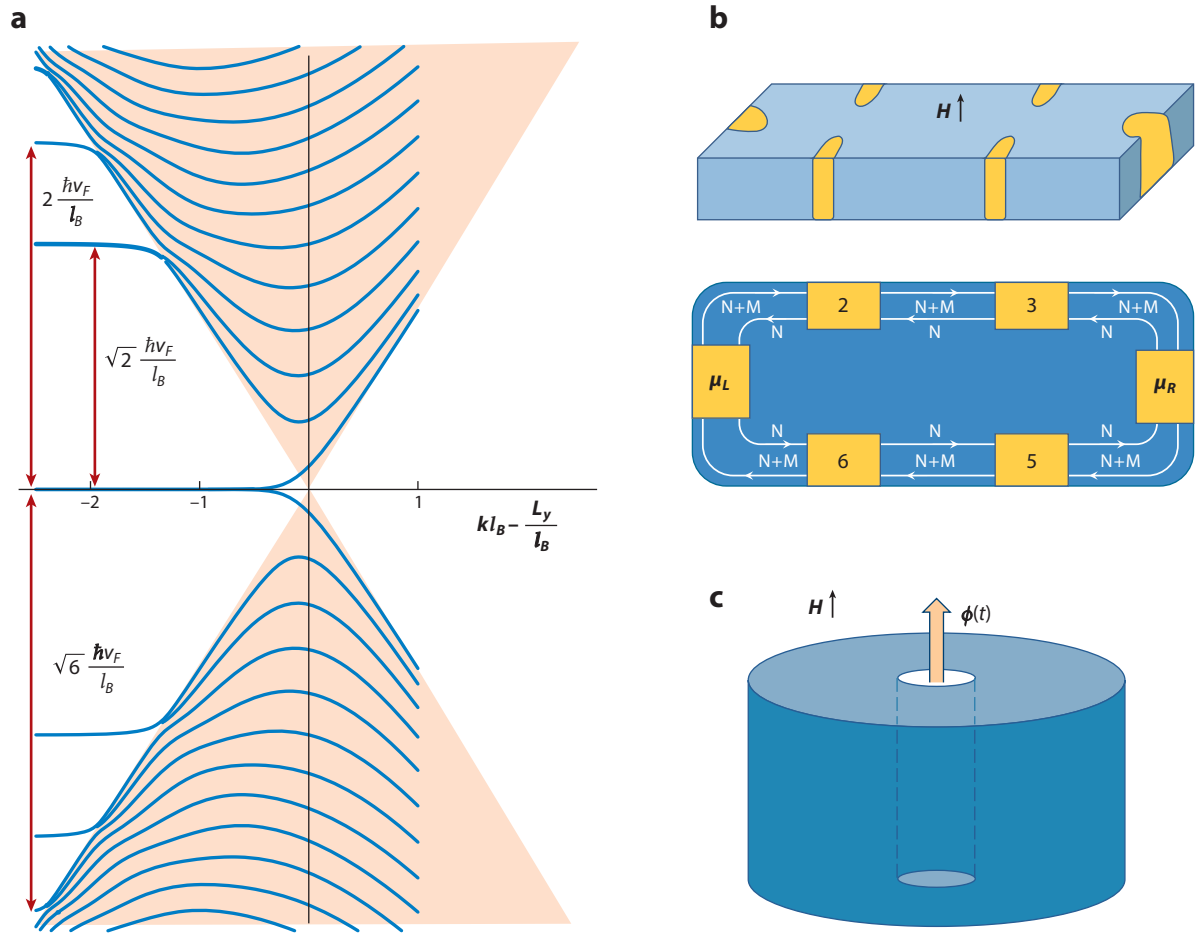

Figure 5

(*a*) Electronic spectrum of a 3D topological insulator semi-infinite slab of finite thickness versus the guiding-center coordinate. Far away from any edges, the spectrum exhibits the usual Dirac Landau level quantization $E = \sqrt{n}\sqrt{2}\hbar v_F/\ell_B$, where the magnetic length is $\ell_B = \sqrt{\hbar c/eB}$, and $\hbar v_F = A_0 \approx 3.3 eV\mathring{A}$ for Bi_2Se_3. Every such Landau level is doubly degenerate. If the Fermi level lies between the two Dirac Landau levels, the edge spectrum contains $M = 2n + 1$ chiral modes in addition to $2N$ nonchiral modes. (*b*) Schematic of a Hall bar geometry in a 3D topological insulator. (*c*) Corbino geometry setup for measurements of quantum Hall conductivity.

a percent, but it does not reach zero. Although this observation awaits a complete theoretical treatment, if the sample is thin then there are only a few nonchiral modes along the side surfaces that may get Anderson localized with sufficient side-surface roughness, leaving only chiral modes at the edges.

Measurement of σ_{xy} in the Corbino geometry is expected to lead to quantization (111, 112). The idea is to perform the analog of the Laughlin thought experiment (112), experimentally realized in 2D electron gas heterostructures in Reference 115. One measures the amount of charge ΔQ transferred from the inner surface to the outer surface in response to the induced electromotive force produced in the azimuthal direction by a slow change in the magnetic flux $\Delta\varphi$ threading the sample. Then $\sigma_{xy} = -c\Delta Q/\Delta\varphi$. For $\sigma_{xy} = n\frac{e^2}{h}$, half of the charge travels through the

top surface and the other half through the bottom surface. An additional advantage of the Corbino setup is that any interaction-driven fractional quantum Hall states formed by the surface electrons can in principle also be detected (115).

If the external electromagnetic potentials are weak, the linear response theory is applicable. Naively, for a noninteracting system with a gap, we expect that at long wavelength and low frequency the response functions simply change, or renormalize, the dielectric constant and the magnetic permeability; after all, the system is a dielectric insulator. Interestingly, a 3D topological insulator gives rise to additional terms in the electromagnetic response, some of which are analogous to axion electrodynamics (116–119).

5.3. $d_{x^2-y^2}$-Wave Superconductivity in Copper Oxides

Low-energy quasiparticles obeying the Dirac equation may also emerge as a consequence of a phase transition associated with the condensation of Cooper pairs. The specific example that we consider here is the so-called $d_{x^2-y^2}$ pairing, which occurs in cuprate high-temperature superconductors (120, 121). In these layered, quasi-2D materials, one may focus on the electronic structure of a single CuO_2 layer. A simple effective Hamiltonian for this system is

$$H = \sum_{\mathbf{k},\sigma} (\varepsilon_{\mathbf{k}} - \mu) c_\sigma^\dagger(\mathbf{k}) c_\sigma(\mathbf{k}) + \sum_{\mathbf{k}} \left(\Delta_{\mathbf{k}} c_\uparrow^\dagger(\mathbf{k}) c_\downarrow^\dagger(-\mathbf{k}) + h.c. \right), \qquad 17.$$

where $\mathbf{k} = (k_x, k_y)$. The normal state dispersion, given by $\varepsilon_{\mathbf{k}}$, describes a closed Fermi surface, centered around (π, π), and equivalent points in momentum space. The anomalous self-energy $\Delta_{\mathbf{k}}$ must in principle be determined from a microscopic theory; because such a theory is currently missing, one proceeds phenomenologically. Assuming time-reversal symmetry, $\varepsilon_{\mathbf{k}} = \varepsilon_{-\mathbf{k}}$, and $\Delta_{\mathbf{k}}$ can be chosen to be real. Because it transforms as $x^2 - y^2$, it must change sign under a 90° rotation and vanish along the Brillouin zone diagonals, where it intersects with the Fermi surface at four inequivalent points. Weak orthorhombic distortions, such as in YBCO, move the points of intersection slightly away from the zone diagonals (122) but do not change the low-energy physics in an important way.

The energy spectrum of the fermionic quasiparticles can be obtained by solving the Heisenberg equation of motion for $c_\uparrow(\mathbf{k})$ and $c_\downarrow^\dagger(-\mathbf{k})$:

$$i\hbar \frac{\partial}{\partial t} \begin{pmatrix} c_\uparrow(\mathbf{k}) \\ c_\downarrow^\dagger(-\mathbf{k}) \end{pmatrix} = \begin{pmatrix} \varepsilon_{\mathbf{k}} - \mu & \Delta_{\mathbf{k}} \\ \Delta_{\mathbf{k}} & -\varepsilon_{\mathbf{k}} + \mu \end{pmatrix} \begin{pmatrix} c_\uparrow(\mathbf{k}) \\ c_\downarrow^\dagger(-\mathbf{k}) \end{pmatrix}, \qquad 18.$$

finding $E(\mathbf{k}) = \sqrt{(\varepsilon_{\mathbf{k}} - \mu)^2 + \Delta_{\mathbf{k}}^2}$. Near the points of intersection between the Fermi surface and the zeros of $\Delta_{\mathbf{k}}$, we may expand $\varepsilon_{\mathbf{k}} - \mu \approx \hbar v_F k_\perp$ and $\Delta_{\mathbf{k}} \approx \hbar v_\Delta k_\parallel$, where $k_\perp$ and $k_\parallel$ are the deviation perpendicular and parallel to the Fermi surface, respectively. In the vicinity of such points, the above has the form of an anisotropic massless Dirac equation.

Interestingly, the Dirac node remains at zero energy even as the chemical potential μ is varied. This is unlike in the previous examples, which involved Dirac particles in semiconductors, where μ must be fine-tuned to coincide with the Dirac node; otherwise we have Fermi circles with finite density of states at zero energy. Furthermore, given that the system is a superconductor, the long-range Coulomb interaction is screened. Since the discovery of cuprates being $d_{x^2-y^2}$ superconductors, there has been a tremendous effort in trying to understand the role of various perturbations. Here we focus on the question of how such a system behaves in an external magnetic field (123–127). The first step toward answering this question is to recognize that the upper and lower components of the spinor in Equation 18 acquire an opposite phase under a $U(1)$ charge

gauge transformation, and therefore, an external magnetic field cannot couple minimally (127–132). Moreover, the pair potential must also be modified. In a mean-field calculation, it is computed self-consistently, with the solution depending on the value of the external magnetic field (124, 126). But even in the absence of a microscopic theory—which may justify a self-consistent mean-field calculation—we can establish this fact by noting that near the transition temperature, the existence of the Ginzburg-Landau functional follows quite generally from the order parameter having the charge $2e$ and the transition being continuous. Given that in cuprates the magnetic penetration depth is much longer than the coherence length, for most of the magnetic field range the field penetrates in the form of flux tubes and the order parameter phase winds by 2π near the core of each vortex. Therefore, in the presence of the external magnetic field, the equation that generalizes Equation 18 is

$$i\hbar\frac{\partial}{\partial t}\begin{pmatrix} c_{\mathbf{r}\uparrow} \\ c^{\dagger}_{\mathbf{r}\downarrow} \end{pmatrix} = \sum_{\mathbf{r}'}\begin{pmatrix} t_{\mathbf{r}\mathbf{r}'} - \mu_{\uparrow}\delta_{\mathbf{r}\mathbf{r}'} & \Delta_{\mathbf{r}\mathbf{r}'} \\ \Delta^{*}_{\mathbf{r}\mathbf{r}'} & -t^{*}_{\mathbf{r}\mathbf{r}'} + \mu_{\downarrow}\delta_{\mathbf{r}\mathbf{r}'} \end{pmatrix}\begin{pmatrix} c_{\mathbf{r}'\uparrow} \\ c^{\dagger}_{\mathbf{r}'\downarrow} \end{pmatrix}, \qquad 19.$$

where we assume that the electrons hop on a square lattice given by $\mathbf{r}$, with a complex amplitude $t_{\mathbf{r}\mathbf{r}'}$. The phase of the complex singlet pair potential $\Delta_{\mathbf{r}\mathbf{r}'}$ winds by 2π when its center-of-mass coordinate encircles a vortex sufficiently far from the vortex core; its dependence on the relative coordinate has $d_{x^2-y^2}$ symmetry.

When the typical separation between vortices, set by $\sqrt{hc/eB}$, is much smaller than the penetration depth, the magnetic field inside is almost uniform. Clearly, in such a case, the plane waves with the wave-number $\mathbf{k}$ are no longer eigenstates of the kinetic energy operator. One may attempt to proceed by working with Landau levels, which, in the continuum limit of the above lattice model, are eigenstates of the kinetic energy operator for a uniform magnetic field (126). However, the number of Landau levels below the Fermi energy, as determined from the quantum oscillations experiments on the overdoped side of the phase diagram (133, 134), is on the order of 10^4 at magnetic fields of 1 tesla, and this number decreases with $1/B$. The energy scale associated with the pair potential is approximately given by $(v_{\Delta}/v_F)E_F$, decreasing the number of Landau levels mixed by $\Delta_{\mathbf{r}\mathbf{r}'}$ by only one order of magnitude. Moreover, the resulting Hamiltonian matrix is dense, prohibiting the use of efficient algorithms for determining the eigenvalues of sparse matrices.

In the relevant magnetic field range $H_{c1} \ll H \ll H_{c2}$, a different approach was proposed by Franz & Tesanovic (127), circumventing the use of the Landau level basis. The idea is to map the problem onto an equivalent problem but at a zero average magnetic field, in which case the plane wave basis may be used. This can be accomplished by performing a singular gauge transformation, familiar in the context of the fractional quantum Hall effect. They then argued that the relevant low-energy excitations reside in the vicinity of the Dirac nodal points and that in the continuum limit, the vortices, together with the magnetic field, act as an effective potential scattering the Dirac particles. As the magnetic field decreases so does the strength of the effective potential, making a natural connection with the zero-field problem. For each of the four massless Dirac particles, which were assumed to be decoupled (125), the combination $\mathbf{v}_F \cdot \left(\frac{\hbar}{2}\nabla\phi - \frac{e}{c}\mathbf{A}\right)$ entered the Dirac equation as an effective electrical potential, Φ (127). Here, $\nabla \times \mathbf{A} = \mathbf{B}$ and $\nabla \times \nabla\phi = 2\pi\hat{z}\sum_j \delta(\mathbf{r} - \mathbf{R}_j)$. The additional minus signs acquired by the quasiparticles upon encircling an odd number of vortices were encoded using a statistical $U(1)$ field minimally coupled to the Dirac particles (127). Such an approach provided an explicit method to (numerically) compute the scaling functions, whose existence was proposed earlier by Simon & Lee (125), as well as to test the validity of the semiclassical approach advanced by Volovik (123).

In the vicinity of each vortex, the effective potential $\frac{\hbar}{2}\nabla\phi - \frac{e}{c}\mathbf{A}$ grows with the inverse of the distance to the vortex. Given that the kinetic energy of a massless Dirac particle also scales with inverse length, the vortices constitute a singular potential. It is therefore not obvious that the long wavelength expansion, which led to the effective Dirac description in the first place, can be directly applied. Indeed, in the continuum limit, one must carefully specify the boundary conditions at the vortex core by requiring that the effective Hamiltonian is a self-adjoint operator (135). A choice of so-called self-adjoint extensions should be determined by matching boundary conditions to a well-regularized lattice theory. Unfortunately, so far it has not been possible to determine their form. Because the choice is not unique and because different physically allowable choices appear to lead to a qualitative difference in the low-energy spectra (e.g., gapped or gapless), one is led to work with the lattice theory (129, 131, 136, 137). The usual choice is to set $t_{\mathbf{rr'}} = -te^{-iA_{\mathbf{rr'}}}$, where the magnetic flux φ through an elementary plaquette enters the Peierls factor via $A_{\mathbf{rr}+\hat{\mathbf{x}}} = -\pi y e\varphi/hc$ and $A_{\mathbf{rr}+\hat{\mathbf{y}}} = \pi x e\varphi/hc$. The ansatz for the pairing term is $\Delta_{\mathbf{rr}+\boldsymbol{\delta}} = \Delta_0 \eta_{\boldsymbol{\delta}} e^{i\theta_{\mathbf{rr}+\boldsymbol{\delta}}}$, where the $d_{x^2-y^2}$-wave symmetry is encoded by $\eta_{\boldsymbol{\delta}} = +(-)$ for $\boldsymbol{\delta}\|\hat{\mathbf{x}}(\hat{\mathbf{y}})$, and the vortex phase factor $e^{i\theta_{\mathbf{rr'}}} = (e^{i\phi_{\mathbf{r}}} + e^{i\phi_{\mathbf{r'}}})/|e^{i\phi_{\mathbf{r}}} + e^{i\phi_{\mathbf{r'}}}|$. This choice is motivated by its behavior in the long-distance limit (129, 138).

For a periodic vortex arrangement, and after the appropriate lattice version of the singular gauge transformation, one can take advantage of the Bloch theorem. The quasiparticle spectrum is then a function of a vortex crystal momentum $\mathbf{q}$. It can be shown that if the vortex lattice has a center of inversion and if the Zeeman term is ignored, then for each eigenstate with an eigenvalue E at $\mathbf{q}$, there is a corresponding eigenstate with an eigenvalue $-E$ at the same $\mathbf{q}$ (131). Therefore, any zero-energy state at a fixed $\mathbf{q}$ must be at least twofold degenerate. However, because our problem breaks time-reversal symmetry, such a degeneracy can only be achieved by fine-tuning an additional parameter other than the two components of $\mathbf{q}$. Therefore, the quasiparticle spectrum of an inversion symmetric vortex lattice is, in general, gapped. The Zeeman term corresponds to a simple overall shift of the quasiparticle energy and does not destroy the avoided crossing but simply moves it to a nonzero energy. Some further nonperturbative aspects of this problem have been discussed in Reference 136.

In **Figure 6**, we show the quasiparticle contribution to the specific heat obtained by the numerical diagonalization of the resulting (sparse) Hamiltonian matrix for different values of magnetic field. The result is rescaled according to the Simon & Lee scaling (125, 138). We see that in the mixed state of a $d_{x^2-y^2}$ superconductor for $v_F/v_\Delta = 7$ and 14, increasing the magnetic field indeed increases the specific heat in an intermediate temperature window, in accord with the semiclassical prediction by Volovik (123). At the lowest temperatures, however, there is a crossover into the quantum regime, where the interference effects set in and the finite spectral gap rapidly decreases the specific heat. Note that the entropy at low T, i.e., $\int_0^T C(T')/T'dT'$, increases with an increasing magnetic field. Entropy must of course be conserved and independent of the magnetic field when $T \to \infty$; the effect comes from the transfer of the spectral weight from energies above $\sim\Delta_0$. It is similar to the effect discussed in the context of the Dirac particle in a periodic electrical potential whose average vanished (see **Figure 2**).

We see then that despite being described by similar kinematics, there is a very important difference in the way the $d_{x^2-y^2}$-wave Dirac particles couple to the physical external magnetic field compared with the way the graphene or the 3D topological quasiparticles couple. In the latter case, the specific heat may oscillate with the field, but when averaged over a few oscillations, its value is field independent. In the former case, it is the average value that increases with the external field.

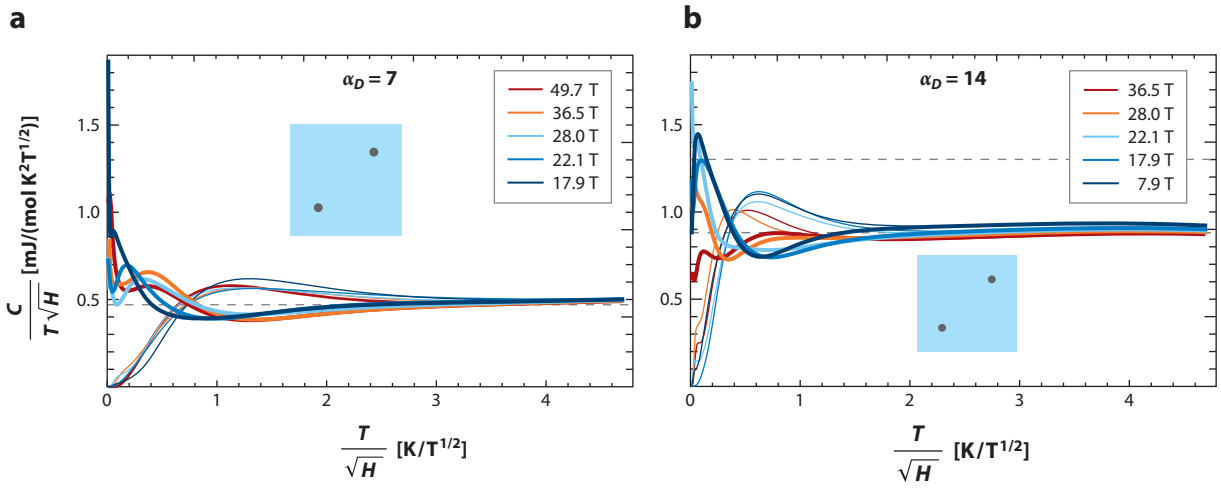

Figure 6

Electronic contribution to the low-temperature specific heat of a $d_{x^2-y^2}$ superconductor in the vortex state (L. Wang & O. Vafek, unpublished results), scaled according to the Simon & Lee scaling (125). The thick lines include the Zeeman term, and the thin lines do not. The electrons hop with the nearest neighbor amplitude t on a tight-binding lattice with a lattice spacing of $a = 3.8\mathring{A}$. The chemical potential was set to $\mu = 0.297t$, corresponding to 15% doping. The Fermi velocity $v_F = 2.15 * 10^5 m/s$ was taken to agree with the photoemission experiments on YBCO (139) by setting $t = 132$ meV. The Dirac cone anisotropy $\alpha_D = v_F/v_\Delta = 7$ in panel *a* and $\alpha_D = 14$ in panel *b*. Insets show the square vortex lattice used. The dashed lines correspond to the values extracted experimentally: In panel *a*, $\sim 0.47\ mJ/molK^2\sqrt{T}$ at 10% doping by Riggs et al. (140); in panel *b*, $\sim 0.87\ mJ/molK^2\sqrt{T}$ at 15% doping by Moler et al. (141) (*lower dashed line*) and $\sim 1.3\ mJ/molK^2\sqrt{T}$ at 15% doping by Wang et al. (142) (*higher dashed line*) (see 143). Abbreviations: T, tesla; *T*, temperature.

6. WEYL SEMIMETALS

> My work always tried to unite the truth with the beautiful, but when I had to choose one or the other, I usually chose the beautiful. - Hermann Weyl (1885-1955)

It has long been known that band touchings in three dimensions are very stable (144, 145), as described in Section 2. When the chemical potential lines up with the band touching points and no other Fermi surfaces intersect it, a semimetal results. The low-energy dispersion of electrons then closely resembles the Weyl equation of particle physics; hence, these semimetals have been termed Weyl semimetals (146). The generic form is shown in Equation 4. Initially, the Weyl equation was believed to describe neutrinos. However, this description had to be given up with the discovery of neutrino mass. Thus, an experimental realization of a Weyl semimetal would be the first physical realization of this fundamental equation. Here we briefly review topological aspects of Weyl semimetals and their possible realizations in solids. For simplicity, consider the following simplified form of Equation 4:

$$H_\pm = \pm v_F(p_x\sigma_1 + p_y\sigma_2 + p_z\sigma_3), \qquad 20.$$

where we have expanded around a pair of band touchings located at $k_\pm$ and have, for example, denoted $p = \hbar(k - k_+)$. The Pauli matrices σ_i act in the space of the pair of bands that approach each other and touch at the Weyl nodes. The energy spectrum then is $E(p) = v_F|\mathbf{p}|$ for both nodes. At each node we can associate a chirality, which measures the relative handedness of the three momenta and the Pauli matrices associated in the Weyl equation. The chirality is ± 1 for the

Hamiltonians $H_{\pm}$. This is a general property of Weyl fermions realized in band structures: Their net chirality must cancel. A simple physical proof of this fermion doubling theorem is pointed out below. In a clean system, where crystal momentum is well defined, one can focus on either node and hence effectively realize the Weyl equation. Note that we have assumed that the bands are individually nondegenerate. This requires that either the time-reversal symmetry or the inversion symmetry (parity) is broken. In order to realize the minimal case of just a pair of opposite chirality Weyl nodes, time-reversal symmetry must be broken (146). In practice, this is achieved by magnetic order in the crystal. Alternately, one may consider systems with broken inversion symmetry (147) in which a minimum of four Weyl nodes are present.

It is useful to describe a toy lattice model in which the above dispersion is simply realized (148, 149). Consider electrons hopping on a cubic lattice, where on every site the electron can be spin up or spin down. Now, assume a spin-orbit-type hopping in the y and z directions that proceeds by flipping spin, while along the x direction the sign of hopping depends on the spin projection. The corresponding Hamiltonian is

$$H(k) = \frac{\hbar v_F}{a}\left(\left[\cos(k_x a) + m\left(2 - \cos(k_y a) - \cos(k_z a)\right)\right]\sigma_1 + \sin(k_y a)\sigma_2 + \sin(k_z a)\sigma_3\right). \quad 21.$$

This Hamiltonian has Weyl nodes located at $(\pm\pi/2a,\ 0,\ 0)$. Linearizing around these points yields the Weyl equation found in Equation 20. Note that one can add an arbitrary (Hermitian) term to this Hamiltonian, which will cause the nodes to shift but cannot remove them for small perturbations. For example, a Zeeman field $\Delta H = -(\hbar v_F/a)h_Z\sigma_1$ shifts the nodes to $(k_{\pm},\ 0,\ 0)$, where $k_{\pm}a = \pm\cos^{-1}h_Z$. Essentially, this stability to perturbations arises from the fact that there is no fourth Pauli matrix available to gap out the node. Only when the field h_Z is large enough $(|h_Z| \geq 1)$ to move the Weyl points up against each other do they annihilate, leading to a fully gapped insulator.

6.1. Topological Properties

The stability of the Weyl nodes is tied to a topological protection inherent to this band structure. Away from the band touching points, there is a clear demarcation between filled and empty bands. Consider the state obtained at a particular crystal momentum by filling the negative energy states (below the chemical potential). By studying how this state evolves via varying the crystal momenta, one can extract a Berry phase, from which a Berry flux, $\mathcal{B}(k) = \nabla_k \times \mathcal{A}(k)$, can be defined. The Weyl nodes are sources, or monopoles, of Berry flux; thus, $\nabla \cdot \mathcal{B}(k) = \pm\delta^3(k - k_{\pm})$, hence their stability. They can only disappear by annihilating a monopole of the opposite charge, which is a Weyl node of opposite chirality (150).

This band topology of Weyl semimetals has two direct physical consequences. The first is an unusual type of surface state, unique to Weyl semimetals, called a Fermi arc (146). Consider a 3D slab of Weyl semimetal with a surface in the x-y plane. Translation invariance along these directions allows us to label single electron states by crystal momenta in this plane. Let us assume we have a single pair of Weyl nodes in the bulk, as in the model in Equation 21. At this same energy, we can ask which surface states are in the system. Surface states are well defined at this energy at all momenta away from the Weyl nodes because there are no bulk excitations with the same energy and momenta. It is easily seen that surface states should form a Fermi arc. The arc terminates at the crystal momenta corresponding to the bulk Weyl nodes (see **Figure 7**). This result follows from the fact that Weyl nodes are monopoles of Berry flux. Therefore, the 2D Brillouin zones that lie between the pair of Weyl nodes have a different Chern number than the planes outside (see **Figure 7**). These planes may be

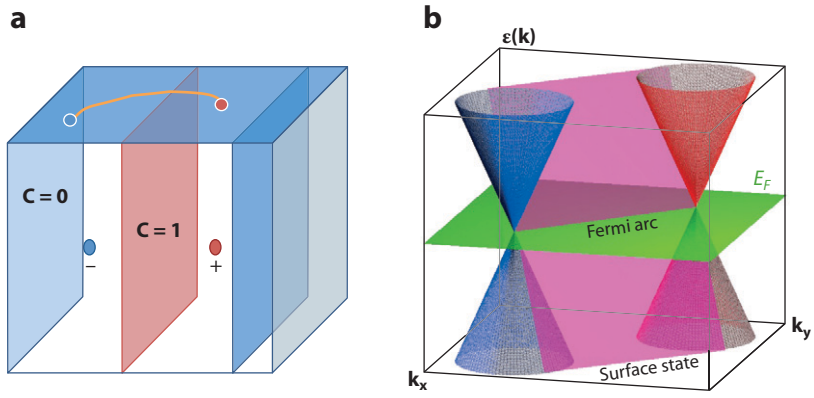

Figure 7

Weyl semimetal. (*a*)The Fermi arc surface states of a Weyl semimetal. (*b*) The bulk dispersion (*red and blue cones*) resolve the paradoxes associated with having Fermi arc states (*shown in pink*) (146). Therefore, Fermi arcs are allowed as surface states of a topological semimetal but are not possible in free fermion band structures in 2D.

interpreted as 2D quantum Hall states associated with a chiral edge state that is guaranteed to cross the chemical potential. The locus of these crossings produces the Fermi arc surface state.

If one considers both top and bottom surfaces of a Weyl semimetal, one should recover a closed Fermi surface as one would expect for a 2D system. Indeed, the two Fermi arc states on opposite surfaces, taken together, form a closed 2D Fermi surface. Thus, a thin slab of semimetal may be viewed as a 2D system with a closed Fermi surface. As the thickness is increased, two halves of this Fermi surface are spatially separated to opposite sides of the sample. Probing these surface states in surface sensitive probes, such as angle resolve photoemission spectroscopy (ARPES) and scanning tunneling microscopy, should provide smoking gun evidence for this unusual phase of matter.

A second physical consequence of the topology of Weyl nodes is their response to applied electric and magnetic fields. As discussed in Section 3, a single Weyl node possesses a chiral anomaly: The net number of charged particles is not conserved if a single Weyl node is present (37, 38), and the continuity equation is modified to

$$\frac{\partial n}{\partial t} + \nabla \cdot J = \pm \frac{1}{4\pi^2}\frac{e^2}{\hbar^2 c}\mathbf{E}\cdot\mathbf{B}, \qquad 22.$$

where the sign is determined by the chirality of the Weyl node. Thus, charge conservation provides a rationale for why Weyl nodes must always occur in a band structure with zero net chirality. Although the net charge is then conserved, the chiral anomaly does lead to an interesting effect. Consider, for example, the case of a pair of nodes with opposite chirality, as in Equation 21. The difference in density between excitations near the two nodes (the valley polarization) is governed by

$$\frac{d(n_+ - n_-)}{dt} = \frac{1}{2\pi^2}\frac{e^2}{\hbar^2 c}\mathbf{E}\cdot\mathbf{B}; \qquad 23.$$

thus, applying parallel electric and magnetic fields can control the valley polarization, which leads to new transport phenomena and possibly even applications for Weyl semimetals. There are close connections between these phenomena and the chiral hydrodynamics recently described in the

high-energy literature (151). A related physical effect is a giant anomalous Hall effect expected for the case of a pair of Weyl nodes, which is proportional to the separation between the Weyl nodes in momentum space. Thus, $\sigma_{yz} = \frac{e^2}{2\pi h}(k_+ - k_-)$. An independent measurement of the momentum separation $(k_+ - k_-)$ between Weyl nodes, obtained, for example, via ARPES, should lead to a quantized ratio of σ_{yz} and $(k_+ - k_-)$. In Weyl semimetals with higher symmetry, such as cubic symmetry, the anomalous Hall conductance vanishes. However, under a uniaxial strain that lowers symmetry, a large anomalous Hall effect is expected (148).

We note that the two topological properties mentioned above require that the Weyl nodes be separated in crystal momentum. In the presence of crystalline translation symmetry breaking, such a distinction may be lost, which would obstruct the definition of a sharp physical property that reflects the underlying topology. Thus, it appears that although semimetals such as the Weyl semimetal may be topological states, the topology associated with them is sharply defined in the presence of translation symmetry, in contrast to insulating topological phases, which do not require any such assumption. However, in practice, disorder is rarely strong enough to completely destroy well-separated nodal points, as evidenced in the example of graphene. Thus, realistic systems should display the novel features mentioned above.

6.2 Physical Realizations

Despite being a very natural band structure, currently there are no clearly established materials with Weyl nodes near the chemical potential, although several promising candidates exist. It has been proposed that members of the family of material $A_2Ir_2O_7$ (pyrochlore iridates), where $A = Y$, or a rare earth such as $A = Eu$, Nd, Sm may be in or proximate to the Weyl semimetal phase (146). This is currently an active area of experimental work (152–155). Spinels based on osmium (156) and $HgCr_2Se_4$ (157) have also been proposed as candidates. Another route has been to try to engineer Weyl semimetals using heterostructures of topological insulators (158, 159). Interestingly, a proposal to realize Weyl points in a photonics band structure has recently appeared (160). A general symmetry analysis of crystal structures that may host Weyl semimetals appeared in Reference 161. Further details on this topic may be found in Reference 162.

7. SUMMARY

We reviewed general conditions under which one may expect gapless Dirac points to occur in solids. Their appearance may be a consequence of band-structure effects or of symmetry breaking due to many-body effects such as superconductivity, or they may appear as a surface state of a bulk topological phase. If a Dirac point exists, additional fine-tuning of the chemical potential is necessary in order for the Dirac point to coincide with the Fermi level, unless the Dirac point appears as a consequence of the condensation of Cooper pairs. Then, the Dirac point rides along with the chemical potential.

We also reviewed how the Dirac fermions respond to externally applied perturbations and why the response differs in the case of graphene, topological insulators, Weyl semimetals, and *d*-wave superconductors. External potentials cause a redistribution of the quasiparticle spectral weight: Space-dependent electrical potential tends to transfer the spectral weight from large energies toward the Dirac point, whereas the Dirac mass term tends to remove the states from the vicinity of the Dirac point, pushing them toward the large energies. A uniform magnetic field redistributes the states over the energy scale set by the cyclotron frequency. In this context, the

magnetic field–induced enhancement of the low-temperature specific heat in the vortex state of *d*-wave superconductors is also reviewed.

When weak, finite-range electron-electron interactions result in only finite renormalization of the Dirac particle dispersion, without leading to any qualitative changes. As the strength of the interactions increases, a quantum phase transition occurs from a semimetal into an insulating state. In the case of the half-filled repulsive Hubbard model on the honeycomb lattice, the transition appears to be into a Néel antiferromagnetic state. Among its attractive features is the possibility to study the transition either using a quantum Monte Carlo method without the fermion sign problem or to analytically use the ε-expansion around $3 + 1$ dimensions for the continuum field theory description, with the massless Dirac particles Yukawa-like coupled to a self-interacting $O(3)$ bosonic field. Understanding why an interacting system may undergo a symmetry-breaking transition into a state with massless Dirac fermions, such as in the cuprate superconductors, rather than avail itself of a fully gapped state, remains a fascinating open problem. Finally, we discussed recent developments of 3D Weyl fermions, including their robust topological properties in the form of unusual surface states and magnetoelectric responses, and their possible physical realizations.

DISCLOSURE STATEMENT

The authors are not aware of any affiliations, memberships, funding, or financial holdings that might be perceived as affecting the objectivity of this review.

ACKNOWLEDGMENTS

O.V. was supported by the NSF CAREER award under grant number DMR-0955561, NSF Cooperative Agreement number DMR-0654118, and the State of Florida. A.V. was supported by ARO MURI grant number W911NF-12-0461.

LITERATURE CITED

1. Dirac PAM. 1928. *Proc. R. Soc. Lond., A Contain. Pap. Math. Phys. Character* 117(778):610–24
2. Wilczek F. 2009. *Nat. Phys.* 5:614–8
3. Weyl H. 1929. *Z. Phys.* 56:330–52
4. Majorana E. 1937. *Nuovo Cim.* 14:171–84
5. Beenakker CWJ. 2013. *Annu. Rev. Condens. Matter Phys.* 4:113–36
6. Nielsen HB, Ninomiya M. 1981. *Nucl. Phys. B* 185:20–40
7. Itzykson C, Drouffe J-M. 1989. *Statistical Field Theory*, Vol. 1. Cambridge, UK: Cambridge Univ. Press, 403 pp.
8. Haldane FDM. 1988. *Phys. Rev. Lett.* 61:2015–8
9. Buttner B, Liu CX, Tkachov G, Novik EG, Brüne C, et al. 2011. *Nat. Phys.* 7:418–22
10. Maciejko J, Hughes TL, Zhang S-C. 2011. *Annu. Rev. Condens. Matter Phys.* 2:31–53
11. Kaplan DB. 1992. *Phys. Lett. B* 288:342–7
12. Kaplan DB, Sun S. 2012. *Phys. Rev. Lett.* 108:181807
13. Volkov BA, Pankratov OA. 1985. *JETP Lett.* 42:178–81
14. Fradkin E, Dagotto E, Boyanovsky D. 1986. *Phys. Rev. Lett.* 57:2967–70
15. Boyanovsky D, Dagotto E, Fradkin E. 1987. *Nucl. Phys. B* 285:340–62
16. Fu L, Kane CL, Mele EJ. 2007. *Phys. Rev. Lett.* 98:106803
17. Fu L, Kane CL. 2007. *Phys. Rev. B* 76:045302
18. Thaller B. 1992. *The Dirac Equation*. New York: Springer-Verlag
19. Ludwig AWW, Fisher MPA, Shankar R, Grinstein G. 1994. *Phys. Rev. B* 50:7526–52
20. Young AF, Kim P. 2011. *Annu. Rev. Condens. Matter Phys.* 2:101–20

21. Schwinger J. 1951. *Phys. Rev.* 82:664–79
22. Allor D, Cohen TD, McGady DA. 2008. *Phys. Rev. D Part. Fields Gravit. Cosmol.* 78:096009
23. Dora B, Moessner R. 2010. *Phys. Rev. B* 81:165431
24. Rosenstein B, Lewkowicz M, Kao HC, Korniyenko Y. 2010. *Phys. Rev. B* 81:041416
25. Gavrilov SP, Gitman DM, Yokomizo N. 2012. *Phys. Rev. D Part. Fields Gravit. Cosmol.* 86:125022
26. Brey L, Fertig HA. 2009. *Phys. Rev. Lett.* 103:046809
27. Castro Neto AH, Guinea F, Peres NMR, Novoselov KS, Geim AK. 2009. *Rev. Mod. Phys.* 81:109–62
28. MacDonald AH. 1983. *Phys. Rev. B* 28:2235–6
29. Lukose V, Shankar R, Baskaran G. 2007. *Phys. Rev. Lett.* 98:116802
30. Jackiw R, Rebbi C. 1976. *Phys. Rev. D Part. Fields* 13:3398–409
31. Rice MJ, Mele EJ. 1982. *Phys. Rev. Lett.* 49:1455–9
32. Su WP, Schrieffer JR, Heeger AJ. 1979. *Phys. Rev. Lett.* 42:1698–701
33. Jackiw R, Schrieffer JR. 1981. *Nucl. Phys. B* 190:253–65
34. Heeger AJ, Kivelson S, Schrieffer JR, Su W-P. 1988. *Rev. Mod. Phys.* 60:781–850
35. Jackiw R, Rossi P. 1981. *Nucl. Phys. B* 190:681–91
36. Weinberg EJ. 1981. *Phys. Rev. D Part. Fields* 24:2669–73
37. Bell JS, Jackiw R. 1969. *Nuovo Cim., A* 60:47–61
38. Adler SL. 1969. *Phys. Rev.* 177:2426–38
39. Bertlmann RA. 1996. *Anomalies in Quantum Field Theory*. New York: Oxford Univ. Press
40. Peskin ME, Schroeder DV. 1995. *An Introduction to Quantum Field Theory*. Cambridge, MA: Perseus Books, 842 pp.
41. Smythe WR. 1950. *Static and Dynamic Electricity*. York, Pa.: McGraw-Hill, 616 pp. 2nd ed.
42. Emelyanenko A, Boinovich L. 2008. *J. Phys. Condens. Matter* 20:494227
43. Wehling TO, Şaşıoğlu E, Friedrich C, Lichtenstein AI, Katsnelson MI, Blügel S. 2011. *Phys. Rev. Lett.* 106:236805
44. Herbut IF. 2006. *Phys. Rev. Lett.* 97:146401
45. Giuliani A, Mastropietro V. 2010. *Commun. Math. Phys.* 293:301–46
46. Giuliani A, Mastropietro V. 2009. *Phys. Rev. B* 79:201403
47. Fisher MPA, Grinstein G, Girvin SM. 1990. *Phys. Rev. Lett.* 64:587–90
48. Herbut IF. 2001. *Phys. Rev. Lett.* 87:137004(4)
49. Gonzalez J, Guinea F, Vozmediano MAH. 1994. *Nucl. Phys. B* 424:595–618
50. Vafek O. 2007. *Phys. Rev. Lett.* 98:216401(4)
51. Sheehy DE, Schmalian J. 2007. *Phys. Rev. Lett.* 99:226–803
52. Herbut IF, Juričić V, Vafek O. 2008. *Phys. Rev. Lett.* 100:046403
53. Mishchenko EG. 2008. *Europhys. Lett.* 83:17005
54. Sheehy DE, Schmalian J. 2009. *Phys. Rev. B* 80:193411
55. Juričić V, Vafek O, Herbut IF. 2010. *Phys. Rev. B* 82:235402
56. Sodemann I, Fogler MM. 2012. *Phys. Rev. B* 86:115408
57. Kotov VN, Uchoa B, Casto-Neto AH. 2008. *Phys. Rev. B* 78:035119
58. Rosenstein B, Lewkowicz M, Maniv T. 2013. *Phys. Rev. Lett.* 110:066602
59. Khveshchenko DV. 2001. *Phys. Rev. Lett.* 87:246802
60. Leal H, Khveshchenko DV. 2004. *Nucl. Phys. B* 687:323–31
61. Herbut IF, Juričić V, Vafek O. 2009. *Phys. Rev. B* 80:075432
62. Sorella S, Tosatti E. 1992. *Europhys. Lett.* 19:699–704
63. Paiva T, Scalettar RT, Zheng W, Singh RRP, Oitmaa J. 2005. *Phys. Rev. B* 72:085123
64. Meng ZY, Lang TC, Wessel S, Assaad FF, Muramatsu A. 2010. *Nature* 464:847–51
65. Sorella S, Otsuka Y, Yunoki S. 2012. *Sci. Rep.* 2:992
66. Assaad FF, Herbut IF. 2013. arXiv:1304:6340
67. Drut JE, Lähde TA. 2009. *Phys. Rev. Lett.* 102:026802
68. Drut JE, Lähde TA. 2009. *Phys. Rev. B* 79:241405
69. Drut JE, Lähde TA. 2009. *Phys. Rev. B* 79:165425
70. Brower RC, Rebbi C, Schaich D. 2011. arXiv:1101.5131 [hep-lat]

71. Brower R, Rebbi C, Schaich D. 2012. arXiv:1204.5424 [hep-lat]
72. Buividovich PV, Luschevskaya EV, Pavlovsky OV, Polikarpov MI, Ulybyshev MV. 2012. *Phys. Rev. B* 86:045107
73. Buividovich PV, Polikarpov MI. 2012. *Phys. Rev. B* 86:245117
74. Ulybyshev MV, Buividovich PV, Katsnelson MI, Polikarpov MI. 2013. arXiv:1304.3660 [cond-mat.str-el]
75. Geim AK, MacDonald AK. 2007. *Phys. Today* 60:35–41
76. Slater JC, Koster GF. 1954. *Phys. Rev.* 94:1498–524
77. Kane CL, Mele EJ. 2005. *Phys. Rev. Lett.* 95:226801
78. Yao Y, Ye F, Qu X-L, Zhang S-C, Fang Z. 2007. *Phys. Rev. B* 75:041401
79. Min H, Hill JE, Sinitsyn NA, Sahu BR, Kleinman L, MacDonald AH. 2006. *Phys. Rev. B* 74:165310
80. Luttinger JM, Kohn W. 1955. *Phys. Rev.* 97:869–83
81. DiVincenzo DP, Mele EJ. 1984. *Phys. Rev. B* 29:1685–94
82. Miller DL, Kubista KD, Rutter GM, Ruan M, de Heer WA, et al. 2009. *Science* 324:924–7
83. Li G, Luican A, Andrei EY. 2009. *Phys. Rev. Lett.* 102:176804
84. Luican A, Li G, Andrei EY. 2011. *Phys. Rev. B* 83:041405
85. Vandecasteele N, Barreiro A, Lazzeri M, Bachtold A, Mauri F. 2010. *Phys. Rev. B* 82:045416
86. Nair RR, Blake P, Grigorenko AN, Novoselov KS, Booth TJ, et al. 2008. *Science* 320:1308
87. Li ZQ, Henriksen EA, Jiang Z, Hao Z, Martin MC, et al. 2008. *Nat. Phys.* 4:532–5
88. Elias DC, Gorbechev RV, Mayorov AS, Morozov SV, Zhukov AA, et al. 2011. *Nat. Phys.* 7:701–4
89. Guinea F, Katsnelson MI, Geim AK. 2010. *Nat. Phys.* 6:30–3
90. Levy N, Burke SA, Meaker KL, Panlasigui M, Zettl A, et al. 2010. *Science* 329:544–7
91. Vozmediano MAH, Katsnelson MI, Guinea F. 2010. *Phys. Rep.* 496:109–48
92. Wang Y, Wong D, Shytov AV, Brar VW, Choi S, et al. 2013. 340:737–40
93. Das Sarma S, Adam S, Hwang EH, Rossi E. 2011. *Rev. Mod. Phys.* 83:407–70
94. Moore JE, Balents L. 2007. *Phys. Rev. B* 75:121306
95. Roy R. 2009. *Phys. Rev. B* 79:195322
96. Zhang H, Liu C-X, Qi X-L, Dai X, Fang Z, et al. 2009. *Nat. Phys.* 6:438–42
97. Liu C-X, Qi X-L, Zhang H, Dai X, Fang Z, et al. 2010. *Phys. Rev. B* 82:045122
98. Hasan MZ, Moore JE. 2011. *Annu. Rev. Condens. Matter Phys.* 2:55–78
99. Harrison W. 1989. *Electronic Structure and the Properties of Solids*. Mineola, NY: Dover Publications, Inc
100. Ando T, Nakanishi T. 1998. *J. Phys. Soc. Jpn.* 67:1704–13
101. Bardarson JH, Twordzyło J, Brouwer PW, Beenakker CWJ. 2007. *Phys. Rev. Lett.* 99:106801
102. Nomura K, Koshino M, Ryu S. 2007. *Phys. Rev. Lett.* 99:146806
103. Lewenkopf CH, Mucciolo ER, Castro Neto AH. 2008. *Phys. Rev. B* 77:081410
104. McCann E, Kechedzhi K, Fal'ko VI, Suzuura H, Ando T, Altshuler BL. 2006. *Phys. Rev. Lett.* 97:146805
105. Aleiner IL, Efetov KB. 2006. *Phys. Rev. Lett.* 97:236801
106. Shon NH, Ando T. 1998. *J. Phys. Soc. Jpn.* 67:2421–9
107. Mucciolo ER, Lewenkopf CH. 2010. *J. Phys. Condens. Matter* 22:273201
108. Schubert G, Fehske H, Fritz L, Vojta M. 2012. *Phys. Rev. B* 85:201105
109. Ostrovsky PM, Gornyi IV, Mirlin AD. 2010. *Phys. Rev. Lett.* 105:036803
110. Bardarson JH, Moore JE. 2012. arXiv:1209.3280 [cond-mat.mes-hall]
111. Lee DH. 2009. *Phys. Rev. Lett.* 103:196804
112. Vafek O. 2011. *Phys. Rev. B* 84:245417
113. Zhang Y-Y, Wang X-R, Xie XC. 2012. *J. Phys. Condens. Matter* 24:015004
114. Brüne C, Liu CX, Novik EG, Hankiewicz EM, Buhmann H, et al. 2011. *Phys. Rev. Lett.* 106:126803
115. Dolgopolov VT, Shashkin AA, Zhitenev NB, Dorozhkin SI. 1992. *Phys. Rev. B* 46:12560–7
116. Wilczek F. 1987. *Phys. Rev. Lett.* 58:1799–802
117. Qi X-L, Hughes TL, Zhang SC. 2008. *Phys. Rev. B* 78:195424
118. Franz M. 2008. *Physics* 1:36
119. Essin AM, Moore JE, Vanderbilt D. 2009. *Phys. Rev. Lett.* 102:146805

120. Van Harlingen DJ. 1995. *Rev. Mod. Phys.* 67:515–35
121. Kirtley JR, Tsuei CC. 2000. *Rev. Mod. Phys.* 72:969–1016
122. Kirtley JR, Tsuei CC, Ariando, Verwijs CJM, Harkema S, Hilgenkamp H. 2006. *Nat. Phys.* 2:190–4
123. Volovik GE. 1993. *JETP Lett.* 58:457–61
124. Wang Y, MacDonald AH. 1995. *Phys. Rev. B* 52:R3876–9
125. Simon SH, Lee PA. 1997. *Phys. Rev. Lett.* 78:1548–51
126. Yasui K, Kita T. 1999. *Phys. Rev. Lett.* 83:4168–71
127. Franz M, Tesanovic Z. 2000. *Phys. Rev. Lett.* 84:554–7
128. Marinelli L, Halperin BI, Simon SH. 2000. *Phys. Rev. B* 62:3488–501
129. Vafek O, Melikyan A, Franz M, Tesanovic Z. 2001. *Phys. Rev. B* 63:134509
130. Vishwanath A. 2001. *Phys. Rev. Lett.* 87:217004
131. Vafek O, Melikyan A, Tesanovic Z. 2001. *Phys. Rev. B* 64:224508
132. Vishwanath A. 2002. *Phys. Rev. B* 66:064504
133. Hussey NE, Abdel-Jawad M, Carrington A, Mackenzie AP, Balicas L. 2003. *Nature* 425:814–7
134. Vignolle B, Carrington A, Cooper RA, French MMJ, Mackenzie AP, et al. 2008. *Nature* 455:952–5
135. Melikyan A, Tesanovic Z. 2007. *Phys. Rev. B* 76:094509
136. Vafek O, Melikyan A. 2006. *Phys. Rev. Lett.* 96:167005
137. Melikyan A, Vafek O. 2008. *Phys. Rev. B* 78:020502
138. Melikyan A, Tesanovic Z. 2006. *Phys. Rev. B* 74:144501
139. Fournier D, Levy G, Pennec Y, McChesney JL, Bostwick A, et al. 2010. *Nat. Phys.* 6:905–18
140. Riggs SC, Vafek O, Kemper JB, Betts JB, Migliori A, et al. 2011. *Nat. Phys.* 7:332–5
141. Moler KA, Baar DJ, Urbach JS, Liang R, Hardy WN, Kapitulnik A. 1994. *Phys. Rev. Lett.* 73:2744–7
142. Wang Y, Revaz B, Erb A, Junod A. 2001. *Phys. Rev. B* 63:094508
143. Fisher RA, Gordon JE, Phillips N. 2007. *Handbook of High-Temperature Superconductivity*, ed. JR Schrieffer, JS Brooks, pp. 326–97. New York: Springer
144. Von Neumann J, Wigner E. 1929. *Phys. Z.* 30:467–70
145. Herring C. 1937. *Phys. Rev.* 52:365–73
146. Wan X, Turner AM, Vishwanath A, Savrasov SY. 2011. *Phys. Rev. B* 83:205101
147. Murakami S. 2007. *New J. Phys.* 9:356
148. Yang KY, Lu YM, Ran Y. 2011. *Phys. Rev. B* 84:075129
149. Delplace P, Li J, Carpentier D. 2012. *Europhys. Lett.* 97:67004
150. Balents L. 2011. *Physics* 4:36
151. Son DT, Yamamoto N. 2012. *Phys. Rev. Lett.* 109:181602
152. Yanagishima D, Maeno Y. 2001. *J. Phys. Soc. Jpn.* 70:2880–3
153. Taira N, Wakeshima M, Hinatsu Y. 2001. *J. Phys. Condens. Matter* 13:5527–33
154. Zhao S, Mackie JM, MacLaughlin DE, Bernal OO, Ishikawa JJ, et al. 2011. *Phys. Rev. B* 83:180402
155. Tafti FF, Ishikawa JJ, McCollam A, Nakatsuji S, Julian SR. 2012. *Phys. Rev. B* 85:205104
156. Wan X, Vishwanath A, Savrasov SY. 2012. *Phys. Rev. Lett.* 108:146601
157. Xu G, Weng H, Wang Z, Dai X, Fang Z. 2011. *Phys. Rev. Lett.* 107:186806
158. Burkov AA, Balents L. 2011. *Phys. Rev. Lett.* 107:127205
159. Halász G, Balents L. 2012. *Phys. Rev. B* 85:035103
160. Ling L, Fu L, Joannopoulos JD, Soljačić M. 2013. *Nat. Photonics* 7:294–9
161. Mañes JL. 2012. *Phys. Rev. B* 85:155118
162. Turner A, Vishwanath A. 2013. arXiv:1301.0330 [cond-mat.str-el]